JGR Solid Earth

RESEARCH ARTICLE
10.1029/2024JB030061

Unraveling the Mantle Dynamics in Central Asia With Joint Full Waveform Inversion

Yajian Gao[1,2], Frederik Tilmann[2,3], Xiaohui Yuan[2], Andreas Rietbrock[1], Sofia-Katerina Kufner[1,4], Wei Li[5], Bernd Schurr[2], and Andreas Fichtner[6]

[1]Now at Karlsruhe Institute of Technology, Karlsruhe, Germany, [2]GFZ Helmholtz Centre for Geosciences, Potsdam, Germany, [3]Freie Universität Berlin, Berlin, Germany, [4]Now at GeoZentrum Nordbayern, Friedrich-Alexander University Erlangen-Nürnberg, Erlangen, Germany, [5]China University of Geosciences (Wuhan), Wuhan, China, [6]ETH, Zürich, Zürich, Switzerland

Abstract We use the full waveform inversion method to study the crustal-mantle seismic structure beneath Central Asia. By combining earthquake waveforms and ambient noise cross-correlations, we construct a 3D model of Vp and Vs down to a depth of 220 km. This model reveals a complex Indian-Asian plate configuration and interaction, resulting from the plate subduction, indentation, and break-off. Beneath the Hindu Kush, the marginal Indian slab with its lower crust is successfully imaged, the latter of which hosts vigorous intermediate-depth seismicity. The subducted marginal Indian slab can be traced further east to the Kohistan Arc, which is a previously undetected structure. We first imaged a flat cratonic Indian plate beneath the Pamir. The indentation of the cratonic Indian plate forces the Asian plate to delaminate, indicated by the south-eastwards dipping high-velocity anomalies, atop which a south-dipping low-velocity zone is observed with higher resolution than previous studies, which we interpret as the delaminated Asian lower crust. In addition, a sharp velocity transition at lithospheric depth is newly discovered and coincides with the Talas-Ferghana fault, delineating the boundary of the Ferghana basin with the Central Tian Shan. Low-velocity anomalies mainly focus beneath the south and northern part of the Central Tian Shan with deep Moho, indicating the lithosphere is possibly delaminated and the deformation of the Central Tian Shan is probably concentrated at the north and south margins by the Tarim basin and Kazakh Shield, respectively. In contrast, West Tian Shan displays a simpler lithospheric structure with a single deep Moho.

Plain Language Summary The ground motion caused by earthquakes can be recorded by seismometers. The recorded seismograms contain information about the seismic structure of the Earth's interior and can also be simulated using the numerical method. The differences between the simulated waveforms and observed ones can be used to update the current seismic speed model. Meanwhile, the background noise mainly caused by the ocean waves also contains information on the shear wave speed beneath the Earth's surface and can also be simulated. Combining these two data sets, we obtained a detailed velocity structure beneath Central Asia, which represents the western corner of the greatest continental collision between the Indian and the Eurasian plates. Our model reveals a subducting slab from the Indian plate side beneath the Hindu-Kush, whereas, beneath the Pamir, the Indian plate lies flat and the Asian plate is pushed beneath the flat Indian plate. In addition, we discovered different structures of the West and Central Tian Shan. The West Tian Shan has a single deep crust-mantle boundary (Moho). In contrast, Central Tian Shan has a more complicated Moho structure, with the south and north parts showing deep Moho, which reflects underthrusting structures from the Tarim basin and Kazakh Shield, respectively.

Key Points:

- Joint full waveform inversion of earthquake waveforms and ambient noise cross-correlations for Central Asia
- The indentation of the cratonic Indian mantle lithosphere promontory and Asian plate delamination are imaged beneath the Pamir
- Marginal Indian plate subduction beneath Hindu Kush and distinct lithospheric structure beneath West and Central Tian Shan are also imaged

Supporting Information:

Supporting Information may be found in the online version of this article.

Correspondence to:

Y. Gao,
ya-jian.gao@kit.edu

Citation:

Gao, Y., Tilmann, F., Yuan, X., Rietbrock, A., Kufner, S.-K., Li, W., et al. (2025). Unraveling the mantle dynamics in Central Asia with joint full waveform inversion. *Journal of Geophysical Research: Solid Earth*, *130*, e2024JB030061. https://doi.org/10.1029/2024JB030061

Received 1 AUG 2024
Accepted 23 JAN 2025

Author Contributions:

Conceptualization: Yajian Gao, Frederik Tilmann, Xiaohui Yuan, Andreas Rietbrock, Wei Li, Bernd Schurr, Andreas Fichtner
Data curation: Yajian Gao, Frederik Tilmann, Xiaohui Yuan, Sofia-Katerina Kufner, Bernd Schurr
Formal analysis: Yajian Gao, Frederik Tilmann, Xiaohui Yuan, Sofia-Katerina Kufner, Wei Li
Funding acquisition: Frederik Tilmann, Xiaohui Yuan, Andreas Rietbrock
Investigation: Yajian Gao, Frederik Tilmann, Xiaohui Yuan, Sofia-Katerina Kufner, Bernd Schurr
Methodology: Yajian Gao, Wei Li, Andreas Fichtner

1. Introduction

The Himalaya-Tibet-Pamir mountain belts (Figure 1) share an evolutional history since about 60 Myr ago (Najman et al., 2010), when the Neo-Tethys Ocean finally closed and the Indo-Eurasian collision began. These connected mountain belts represent the largest active continental collision zone on Earth (Rutte et al., 2017). The major morphotectonic provinces of the study area include the Pamir, Hindu Kush, and Tian Shan mountain belts, the Tajik, Ferghana, and Tarim basins, as well as the Kohistan and Ladakh arcs (Figure 1).

The Tian Shan orogeny (Figure 2), as one of the most active and largest intracontinental orogenic zones on Earth, was initiated in the Late Paleozoic as a result of the convergence of the Paleo-Asian Ocean and multiple subduction accretions in the late Paleozoic, with deformation lasting until the Mesozoic (Burtman, 2015; Xiao

Project administration: Frederik Tilmann, Xiaohui Yuan, Andreas Rietbrock
Resources: Yajian Gao, Frederik Tilmann, Xiaohui Yuan, Bernd Schurr, Andreas Fichtner
Software: Yajian Gao, Andreas Fichtner
Supervision: Frederik Tilmann, Xiaohui Yuan, Andreas Rietbrock
Validation: Yajian Gao
Visualization: Yajian Gao, Frederik Tilmann, Wei Li
Writing – original draft: Yajian Gao
Writing – review & editing: Yajian Gao, Frederik Tilmann, Xiaohui Yuan, Andreas Rietbrock, Sofia-Katerina Kufner, Wei Li, Bernd Schurr, Andreas Fichtner

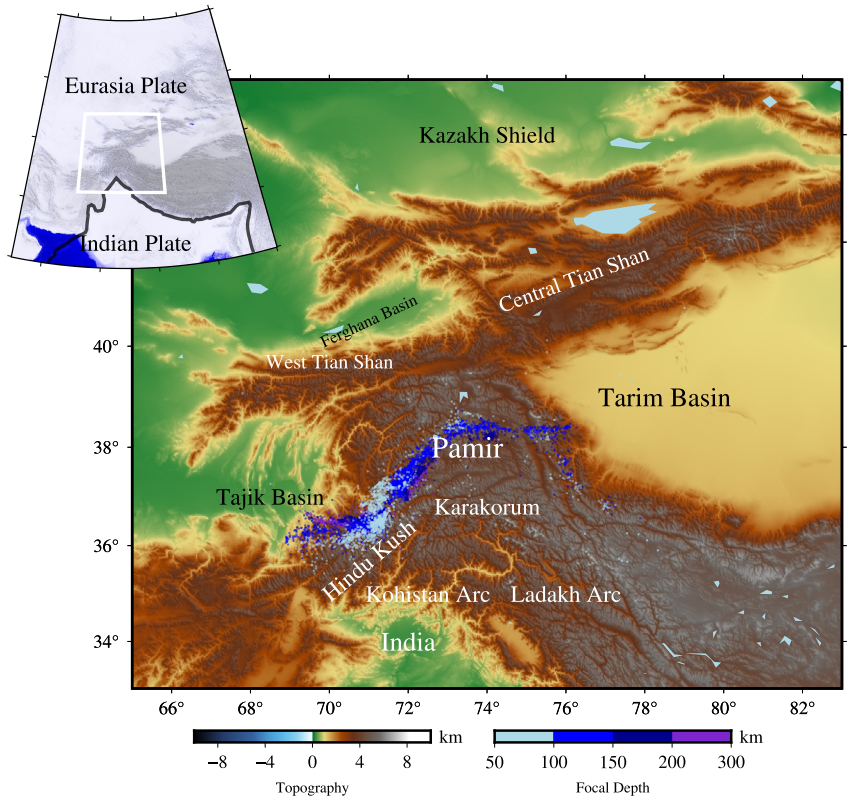

Figure 1. Map showing the study region and intermediate-depth seismicity (>50 km) distribution for Central Asia. The intermediate-depth seismicity is retrieved from Kufner et al. (2017) and Bloch et al. (2021). The Tian Shan is divided into West and Central Tian Shan in this study. The inset on the left upper corner shows the Indian-Asian collision zone for context. The thick black line denotes the boundary of the Indian plate at the surface.

et al., 2013). It was reactivated since ~25–20 Ma in response to the far-field effects of the Indian and Eurasian collisions (Yin et al., 1998). The Tian Shan is characterized by rugged topography, high peaks, and deep valleys. It can be divided into East, Central, and West Tian Shan, each with distinct geological features. The Talas-Ferghana Fault is a major strike-slip fault that significantly influences the geology of the area and separates the Central Tian Shan from the Ferghana Basin and West Tian Shan.

The Pamir (Figure 2) is bounded by the sinistral Darvaz Fault to the west, the Main Pamir Thrust to the north, and the dextral Karakorum Fault and Kashgar-Yecheng Fault System to the east. The Sarez-Karakul Fault System divides the Pamir into western and eastern parts, the west is characterized by deep valleys and high mountains, whereas the east is characterized by a plateau (Schurr et al., 2014). Pamir has a crust up to 80 km thick (e.g., Q. Xu et al., 2021; Schneider et al., 2019) and its lithospheric terranes can be paired with an equivalent amalgamation of terranes in Tibet, comprising Gondwana-derived micro-continents, subduction-accretion complexes, and arcs (Robinson et al., 2012). These terrane units were accreted to Asia during the Paleozoic and Mesozoic and are nowadays separated by northward convex sutures (Schwab et al., 2004), namely the North Pamir-Kunlun Suture, the Akbaytal–Tanymas suture, and the Rushan-Pshart suture, which outline an orocline and are the basis for the subdivision of Pamir into the North, Central, and South Pamir (Figure 2). Geographically, south of the South Pamir are the Tajik Pamir and Karakorum, which are separated by the Shyok Suture from the Kohistan-Ladakh Arc. The western and eastern flanks of the Central and South Pamir are named West and East Pamir, respectively. Further west and east are the Afghan Pamir and Chinese Pamir. The Central and South Pamir crust experienced Cenozoic high-grade metamorphism and magmatism. The related rock outcrops have been discovered in extensional gneiss domes: the Yazgulom, Sarez, Muskol, and Shatput domes in Central Pamir; the Shakhdara dome in the South Pamir; and the Kongur Shan and Muztaghata domes in the East-Chinese Pamir (Rutte et al., 2017; Schmidt et al., 2011; Schneider et al., 2019). Compared to the equivalent Tibetan terranes, the Pamir terranes were translated northward by around 300 km (Burtman & Molnar, 1993), and have a much reduced

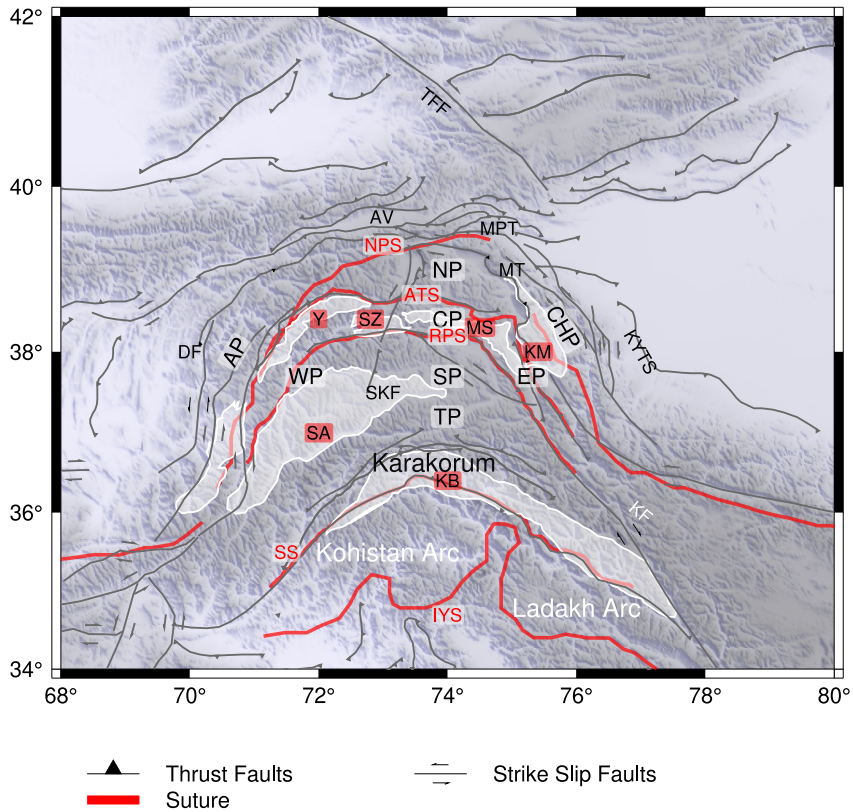

Figure 2. Map of geological features in the study area. Sutures are indicated by the red lines: North Pamir/Kunlun Suture (NPS), Akbaytal–Tanymas Suture (ATS), Rushan–Pshart Suture (RPS), Shyok Suture (SS), Indus-Yarlung (IYS). ATS and RPS separate the Pamir into North Pamir (NP), Central Pamir (CP) and South Pamir (SP). South of SP are the Tajik Pamir (TP), Karakorum, Kohistan Arc and Ladakh Arc. The western flank of the Pamir can be further divided into West (WP) and Afghan Pamir (AP) whereas the eastern flank is named East (EP) and Chinese Pamir (CHP). Large faults in gray include Main Pamir Thrust (MPT), Muji-Tashkorgan Graben System (MT), Talas-Ferghana Fault (TFF), Darvaz Fault (DF), Kashgar-Yecheng Fault System (KYTS), Karakorum Fault (KF), Sarez-Karakul Fault System (SKF). White shaded areas outline the Cenozoic gneiss domes of the Pamir including Yazgulom (Y), Sarez (SZ), Muskol-Shatput (MS), Kongur Shan-Muztaghata (KM), Shakhdara-Alichur (SA) and Karakoram Batholith (KB). The Pamir is separated from Tian Shan by the Alai Valley (AV). Major faults are collected from the Central Asia Fault Database (Mohadjer et al., 2016) from website (https://faults.smohadjer.de/), sutures and domes are retrieved from Kufner et al. (2016), W. Li et al. (2018), Schneider et al. (2019), Kumar et al. (2022), and Chapman et al. (2018).

latitudinal extent, suggesting shortening by up to 60% in the north-south direction (Waldhör et al., 2001; Schmidt et al., 2011; W. Li et al., 2018). The shortening in the Pamir promotes lateral extrusion and deep subduction of the crust in the Hindu Kush and Pamir (Kufner et al., 2017; W. Li et al., 2018). The Hindu Kush is located southwest of the Pamir orogen and south of the Tajik Basin, containing the Paleozoic suture zone in the center and existing as a subduction-type orogen before the Indian-Asia collision (Treloar & Izatt, 1993). Different from the Pamir, the indentation of the Indian plate did not cause a significant northward offset in the Hindu Kush, but instead, the collision initiated the formation of strike-slip faults, and the displacement was translated via transfer systems into the Central Pamir (Kufner, Schurr, et al., 2018; Schurr et al., 2014).

Different from Tibet, the Hindu Kush and Pamir host vigorous intermediate-depth seismicity, reaching a depth of about 250 km in the Pamir and 300 km in the Hindu Kush, common in oceanic subduction zones but rare in continental collision environments mainly due to the scarcity of hydrous minerals in the continental mantle lithosphere compared to the oceanic subduction zones (Bloch et al., 2021, 2023; Kufner et al., 2017, 2021; Sippl et al., 2013).

In previous tomographic studies, a northward dipping slab break-off in the deep upper mantle (down to 200–300 km) has been imaged beneath the Hindu Kush (Koulakov & Sobolev, 2006; Kufner et al., 2016, 2017, 2021; Replumaz et al., 2010), which was interpreted as the thin and extended western continental margin of the Indian

plate (marginal India) by Kufner et al. (2016). Therefore, marginal India's crust and denser lithosphere are supposed to be separated from Cratonic India and subducted beneath the Asian plate. In contrast, the Asian plate is subducting southward and eastward beneath the Pamir crust (Sippl et al., 2013). Receiver function studies (Schneider et al., 2013) revealed a double Moho beneath the Central Pamir, which links to delamination of the Asian continental lower crust. The shallower Moho is around 70 km, whereas the deeper Moho deepens southward, forming a south-dipping feature. The double Moho is also detected beneath the East-Chinese Pamir, suggesting the eastward underthrusting of the Pamir lower crust beneath the East-Chinese Pamir (Q. Xu et al., 2021).

Most of the previous studies including tomography and receiver functions were based on temporary, spatially restricted networks, lacking a comprehensive impression of the entire study domain. Teleseismic tomography cannot easily separate anomalies in the crust and uppermost mantle or near horizontal layers due to smearing along nearly vertical ray paths, such that starting model and crustal corrections exert a strong influence on final results (Kufner et al., 2016, 2021). Local and regional travel-time earthquake tomography (Sippl et al., 2013) can only provide details for the crust and upper mantle in the selected regions but lacks resolution at larger depths. Surface wave tomography (Kumar et al., 2022; W. Li et al., 2018; Liang et al., 2020) provides large-scale crustal and uppermost mantle images, however, the resolution is limited. Surface waves are primarily sensitive to shallow structures, and the technique often relies on the fundamental mode of surface waves, neglecting the higher-order multimode signals that are essential for imaging deeper structures. Additionally, the frequency band limitations and simplified assumptions based on 1D sensitivity kernels further constrain its resolution compared to 3D surface wave full waveform inversion (Wang et al., 2018).

In this study, we employ a joint full waveform inversion (FWI) scheme to recover the seismic structure below the Hindu Kush, Pamir, and Tian Shan regions. We include the seismic waveforms from intermediate-magnitude earthquakes in the study area and vertical component cross-correlation empirical Greens' Functions extracted from the ambient noise. Accurate numerical simulations of seismic wave propagation (e.g., Afanasiev et al., 2019; Komatitsch & Tromp, 2002) through laterally heterogeneous models allow the modeling and inversion of complex waveforms with the adjoint method (e.g., Chen et al., 2015; Fichtner et al., 2010; Gao, Yuan, et al., 2021; Rodgers et al., 2024), providing abundant information related to the structure of the Earth. Advances in computational power make it feasible to invert full waveforms to image the seismic structure at regional scales down to relatively short periods, here 10 s with a spatial resolution down 20 km.

Our detailed 3-D velocity model reveals the continental subduction of the Indian plate beneath the Hindu Kush and the Asian plate subducting below the Indian plate beneath the Pamir. Meanwhile, our model also provides first-order constraints for future thermomechanical numerical models and may help to explain the lateral variations in the exhumation rules and collision style revealed by the geological records. Our model is also useful for earthquake relocation, moment tensor inversions, and physics-based ground motion estimations (Kufner et al., 2023).

2. Data

Seismic waveforms were recorded by 21 permanent and temporary networks deployed at various periods between 1982 and 2019 (Figure 3a and Table S1 in Supporting Information S1) including 18 broadband networks and 3 short-period networks (which are only used for P wave FWI of higher frequency stages). We collected centroid locations, origin times, and moment tensors for 200 earthquake events with magnitudes between M_W 5.0 and 7.0 within the study region from the Global Centroid Moment Tensor Catalog (GCMT) (Ekström et al., 2012). From these 95 events were recorded clearly by at least 20 stations.

As pre-processing, the instrument responses were removed from the raw seismic data to obtain ground displacement. For each stage of the inversion, third-order Butterworth band-pass filters with corresponding filtering bands were applied (see Section 3). Then at each stage, we made visual checks of the remaining events and removed waveforms, which are noisy or showed obvious signs of cycle skipping compared to synthetics computed with the current model. Events that did not provide waveforms for at least 20 stations (or at least 20 broad-band traces) after this visual inspection were also removed. Removal of events with few useable records is helpful as the computational cost of FWI scales with the number of events, and a practical approach is therefore to maximize the amount of seismic waveform data for every event used in the study (Krischer et al., 2018).

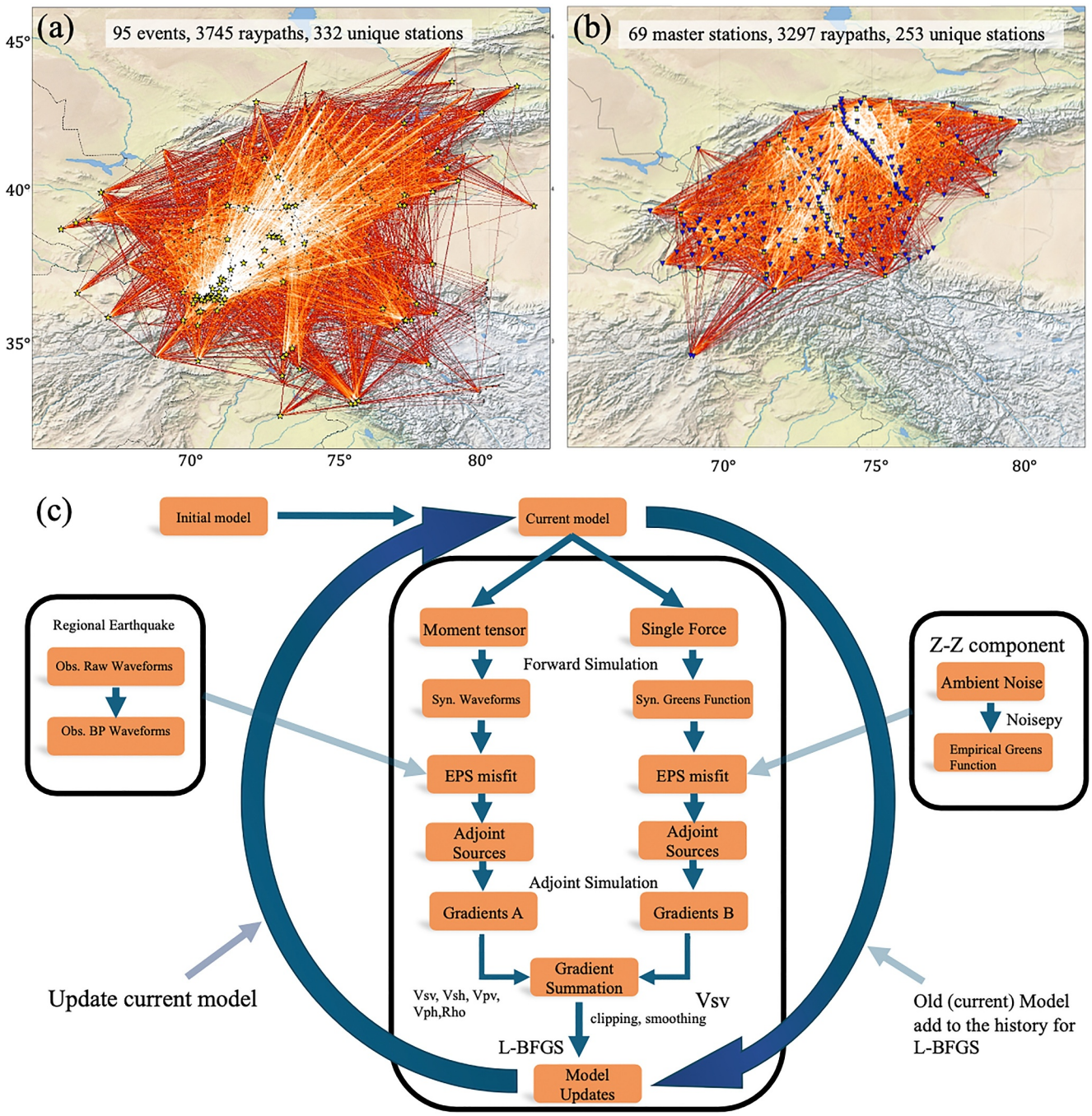

Figure 3. (a) Ray path coverage for earthquake data and (b) EGFs. Yellow stars in (a) denote the earthquake centroid locations while yellow triangles in (b) denote the master stations used as virtual sources. (c) Joint FWI workflow including earthquake waveforms and EGFs. The ray path coverage for the validation data set is illustrated in Figure S1 in Supporting Information S1.

Furthermore, high-quality empirical Greens' Functions (EGFs) were derived from cross-correlations of the vertical components of continuous seismic data for station pairs (Wang et al., 2018). We include 1,476 pairs of stations (18 networks) from 233 unique stations and select 69 master stations as virtual sources for forward simulations, covering the study domain (Figure 3b and Table S1 in Supporting Information S1). To extract reliable Rayleigh wave signals, we first cut the continuous seismic data into 12 hr long segments and removed the instrument response, then resampled the data to 1 Hz. To mitigate the effects of nonstationary phases caused by earthquakes, time- and frequency-domain normalization are commonly used. In this work, we use Noisepy (Jiang

& Denolle, 2020) to apply the two-step spectral whitening including frequency-domain normalization and running-mean average (RMA). The spectrally whitened continuous waveforms are then further split into 800 s long segments which are then cross-correlated for station pairs in the Fourier domain. The cross-correlation waveforms of the ZZ components are linearly stacked. The EGFs are then obtained as the negative time derivatives of the stacked cross-correlation waveforms between each station pair. In this study, only ZZ components are used due to the simplicity of the reciprocity of Greens' functions for vertical components.

3. Methods

The waveform modeling for earthquake waveforms and EGFs is accomplished by Salvus (Afanasiev et al., 2019), which is a suite of highly parallelized spectral-element solver of the seismic wave equation which includes anisotropy, attenuation, ellipticity and topography.

3.1. Parameterization and Starting Model

The model is parameterized into velocities for vertically and horizontally propagating P waves (V_{PV} and V_{PH}) and vertically and horizontally polarized S waves (V_{SV} and V_{SH}), density ρ and bulk attenuation Q_κ and shear attenuation Q_μ. We extract an initial model from SP12RTS (Koelemeijer et al., 2015) and set $V_{SV} = V_{SH} = V_S$ and $V_{PV} = V_{PH} = V_P$ to represent the isotropic velocity of SP12RTS. The SP12RTS is an isotropic V_S and V_P tomography velocity model based on four million Rayleigh wave dispersion, 300,000 shear wave travel times, 400,000 P wave travel times, and 7,000 normal mode splitting function coefficients.

To reduce the possible bias from fixing density (Blom et al., 2017; Płonka et al., 2016), we update the density in all iterations but abstain from its interpretation due to the inferior resolution compared to the seismic velocity parameters. Attenuation is fixed based on PREM model values (Dziewonski & Anderson, 1981) through the whole inversion because only the relative amplitudes and phase shifts are used.

In this paper, we translate the V_{SV} and V_{SH} into isotropic V_S through the Voigt average (Panning & Romanowicz, 2006) for the final model, as the retrieved radial anisotropy might suffer from bias due to unevenly distributed ray paths. We will only focus on the interpretation of isotropic V_S, which is better resolved than V_P due to several factors, including the frequency range of the inversion, the larger amplitude of S and surface waves compared to P waves, and the additional contributions of the Rayleigh waves from the EGFs, which are predominantly sensitive to V_S. However, we also present, without interpretation, the isotropic V_P model and radial anisotropy in Supporting Information S1.

The spectral element mesh is shown in Figure S2 in Supporting Information S1, where the element size is adapted based on the inversion period and relevant wavelength (with two elements per wavelength). In the crust, this design results in the smallest element size of approximately 12 km, which allows the mesh to capture crustal structures effectively. The medium wavelength surface topography from the EGM2008 Geoid (Pavlis et al., 2012) and Earth2014 global topography model (Hirt & Rexer, 2015) with Earth ellipticity according to WGS84 and the Moho topography of Crust1.0 (Laske et al., 2013) are implemented by deforming the mesh grid vertically and adding additional refined elements (Figure S2 in Supporting Information S1). The surface topography has been filtered with the maximum angular order lmax = 1,024, equivalent to a spatial resolution of 20 km to fully consider the topography complexity of the study domain. The maximum angular order for the Moho topography is lmax = 128 equivalent to the spatial resolution of 155 km to interpolate the initial model SP12RTS (Koelemeijer et al., 2015).

3.2. Forward Modeling of Earthquake Waveforms and Empirical Greens' Functions (EGFs)

For earthquake simulations, the band-passed Heaviside source time function is applied, with the bandpass corners set according to the different inversion stages. For the simulation of the EGFs, we use a Gaussian source time function (Wang et al., 2018) injected at selected master stations as virtual sources and assume that the distribution of ambient noise sources is homogeneous. Due to the inland environment of Central Asia, the potential bias effects on the EGFs from non-uniform primary microseism source distributions are expected to be small and averaged through the stacking of over 1-year (Kumar et al., 2022; Lü et al., 2019, 2021).

To reduce the effects of uneven coverage of seismic stations and events, we integrate event and station weightings into the inversion, following the geographical weighting scheme from Ruan et al. (2019).

3.3. Multi-Scale Joint Inversion of Earthquake Waveforms and EGFs

Before introducing the inversion workflow and results, we introduce three misfit functions used here. Their performance for different scenarios and seismic phase types has previously been evaluated (Gao et al., 2023; Y. Yuan et al., 2020). The time-frequency phase shift (TFPS), which was suggested by Fichtner et al. (2008) and Kristeková et al. (2009), measures the instantaneous phase shift between synthetic seismograms and recorded seismograms in the time-frequency domain. The exponentiated phase shift (EPS) was designed to alleviate the poor fitting of scattered waves due to phase discontinuities (jumps) in the time domain caused by the instantaneous phase shift (IPS) (Y. Yuan et al., 2020). EPS employs the Hilbert transform but calculates the waveform differences in the real and imaginary parts and is therefore not affected by phase jumps.

The cross-correlation-coefficient (CCC) shares the simplicity of the least-squares misfit and is defined as the vector product between the normalized observed and synthetic data (Gao, Tilmann, et al., 2021; Tao et al., 2017). The normalization term gives equal weight to each time window, regardless of its absolute amplitude, which can be affected by uncertainties in the source parameters or receiver side effects. However, it retains the relative amplitudes within a time window that helps to constrain the sharp boundary of the velocity anomalies; this information is prone to be ignored by the exclusively phase-based measures of misfit.

Based on multi-scale adjoint earthquake FWI (e.g., Gao, Tilmann, et al., 2021; Krischer et al., 2018; Wehner et al., 2022), we initiate the inversion from long-period data (60–100 s) using the TF as misfit function, then gradually extend the period range to 20–100 s through four stages encompassing 25 iterations in total (Figure 4a). We then switch to using the CCC to measure the relative amplitudes for the inversion of the shortest period, 15–100 s in the fifth stage and 12–100 s in the sixth (Figure 4a and Figure S3 in Supporting Information S1). Because the CCC is better suited to capture the waveform distortions from multi-pathing or scattering after most of the phase shifts have already been eliminated through the previous iterations (Gao, Yuan, et al., 2021; Tao et al., 2017). The inversion is driven by the limited-memory Broyden–Fletcher–Goldfarb–Shanno algorithm (L-BFGS) (Liu & Nocedal, 1989) following Gao, Tilmann, et al. (2021). From periods 20–60 s (iteration 17), we simulate the EGFs and calculate the misfits between the EGFs and the synthetic Greens' functions using both TFPS (Fichtner et al., 2008) and EPS (Y. Yuan et al., 2020) but do not yet use the EGFs for model updates. Both misfit evolutions show similar patterns, but the TFPS is more sensitive to the previous model evolution (Figure 4b).

For the joint inversion stage (from iteration 48, earthquake FWI:10–100 s and EGFs FWI:15–60 s), the most difficult part is the correct processing of the misfit derivatives for the different data types with respect to the model parameters (here misfit kernel). For the Rayleigh wave phases, the optimal misfit function is the TFPS which is especially suited for model updates during the long period stages, where the improvements in waveform fits are mainly due to decreases in phase shift. However, for the earthquake FWI at shorter periods, we expect to extract more information about the interfaces of seismic anomalies from multi-pathing or scattering.

Previous synthetic tests (Gao et al., 2023; Y. Yuan et al., 2020) demonstrated the robustness of EPS in improving the resolution for both body wave and surface wave FWI. Thus, to comprise the relative amplitude measurements for earthquake body waves and the phase shift measurements for both earthquake and EGF surface waves, we use the EPS as the misfit function to calculate the misfits and adjoint sources for both data sets. We also calculate the TFPS for the EGFs to monitor the misfit evolution (Figures 3 and 4). During the joint inversion, the effective Rayleigh wave windows are selected from the EGFs and provide the phase shift misfit kernel for V_{SV} parameter updates and they are added to the V_{SV} kernels of the earthquakes data set. Therefore, only V_{SV} is jointly inverted using both data sets (Figure S4 in Supporting Information S1), whereas other parameters are constrained from the earthquake data. The detailed workflow is illustrated in Figure 3c.

3.4. Resolution Analysis

Uncertainty analysis for FWI is a challenging task, especially for the multi-parameter cases in seismology where the cross-talking among parameters needs to be quantified. Instead of a computationally expensive synthetic model recovery test, this study employs the computationally affordable and robust method of calculating point-spread functions (PSFs), which is approximated by the Hessian-vector product $\mathbf{H}\delta\mathbf{m}$ at the global minimum. Specifically, we approximate the Hessian-vector multiplication through finite differences of two gradients by perturbing the final model with a model variation test vector $\delta\mathbf{m}$ and obtaining the difference in the gradients

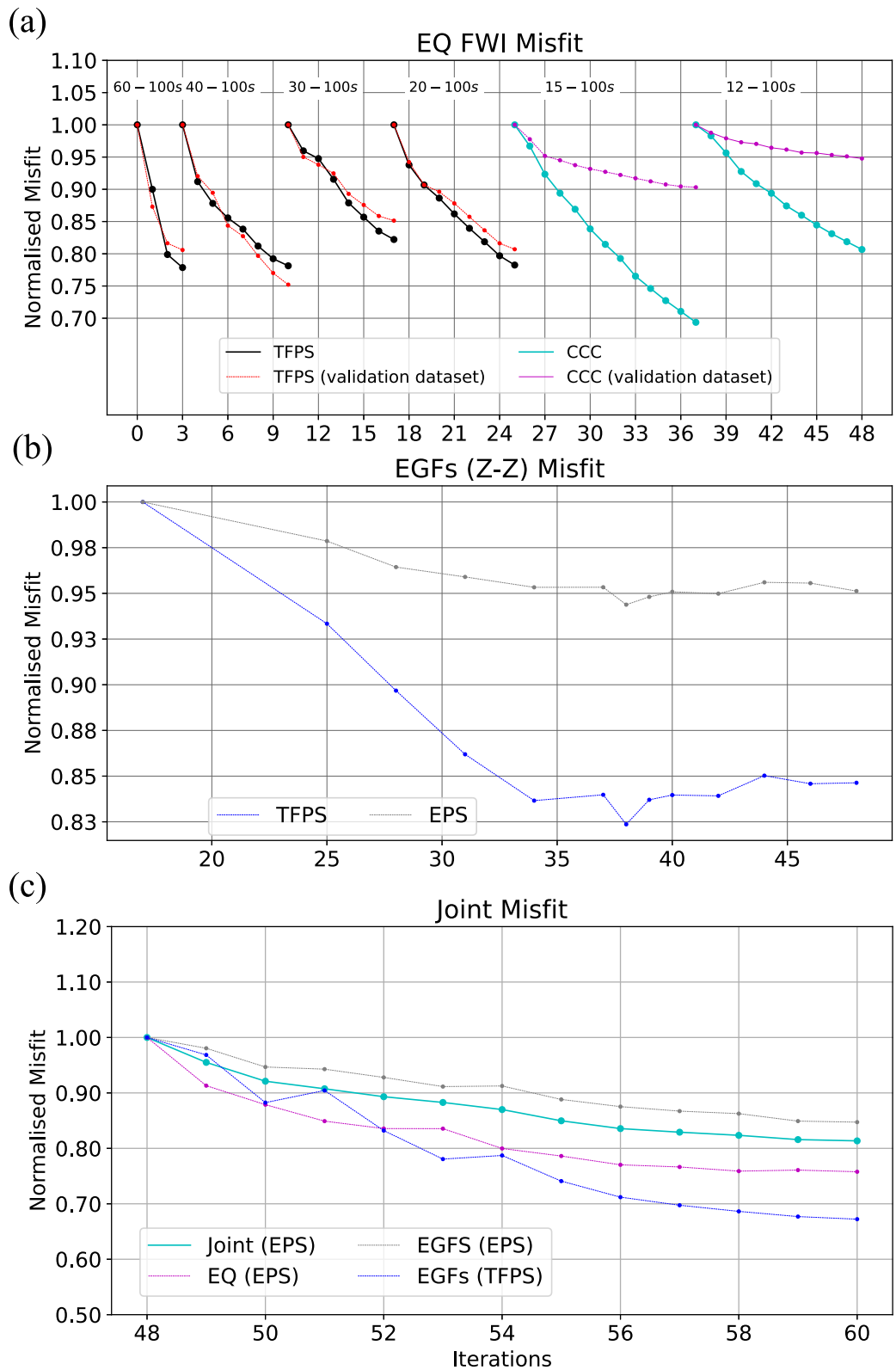

Figure 4. (a) Misfit evolution for the joint FWI including earthquake waveforms and EGFS retrieved from ambient noise data. The top-left panel shows the misfit evolution for the long-period earthquake FWI for the first 48 iterations. (b) Misfit evolution for the 20–60 s EGFs from iteration 17–48. (c) Misfit evolution for the joint inversion process with both types of misfit functions for cross-validation.

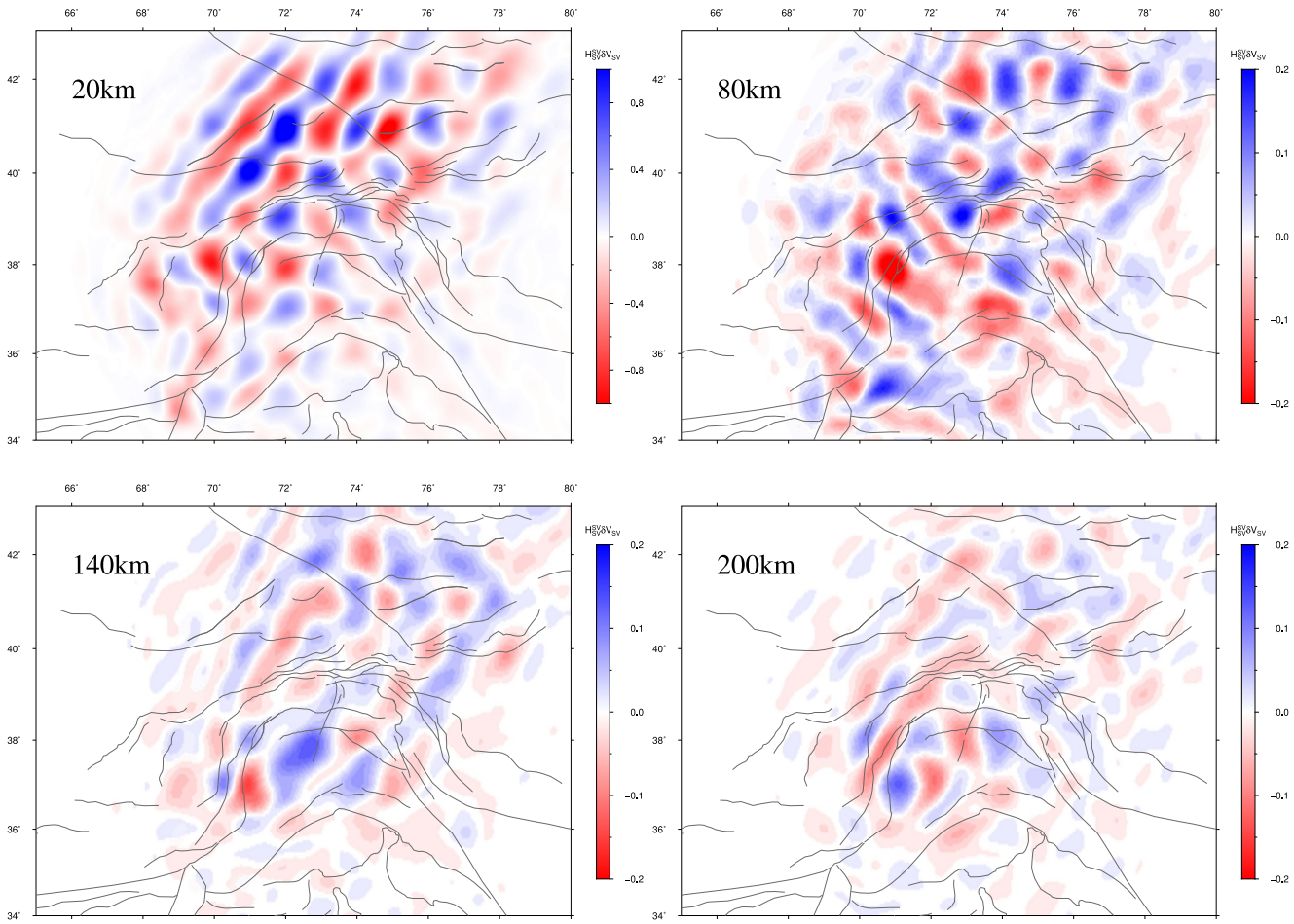

Figure 5. Point-spread function for the V_{SV} at 20, 80, 140, and 200 km based on the joint inversion.

(Fichtner & Leeuwen, 2015; Fichtner & Trampert, 2011; Gao, Yuan, et al., 2021; Tao et al., 2018; Zhu et al., 2015, 2017):

$$\mathbf{H}\delta\mathbf{m} \approx \mathbf{g}(\mathbf{m}+\delta\mathbf{m}) - \mathbf{g}(\mathbf{m}) \quad (1)$$

where $\mathbf{g}(\mathbf{m})$ denotes the summed gradient from the adjoint simulations for model $\mathbf{m}$, whereas $\mathbf{g}(\mathbf{m}+\delta\mathbf{m})$ indicates the gradient from the perturbed model $\mathbf{m}+\delta\mathbf{m}$. $\delta\mathbf{m}$ can be chosen to be visually interpretable, for example, a checkerboard pattern. We note that this approach represents a conservative estimate of the resolution due to the limited number of iterations lacking the simulation of the curvature of the misfit evolutions. Our study involves two different data sets and three types of model parameters, therefore we performed separate resolution tests for each parameter and additional tests for two data sets.

To assess the resolution in the crust and upper mantle, we calculate the V_{SV}-PSFs for the earthquake data and EGF data set separately. We carry out perturbation tests for both data sets at two different scales to distinguish the resolution for the crust and upper mantle. Specifically, we perturbed the V_{SV} model by adding velocity perturbations ($\delta\mathbf{m}$) in a three-dimensional checkerboard pattern in the crust and upper mantle made up of Gaussian spheres with ±1% maximum amplitude of the velocity for a specific depth. To assess the resolution of the upper mantle, a Gaussian width σ of 30 km is used for the test. The horizontal and depth grid spacing of the Gaussian spheres is 2° with an 80 km depth interval starting from 60 km depth. For the higher-resolution test focused on crustal structures, we use $\sigma = 20$ km and a grid spacing of 1° horizontally and 60 km vertically. The joint PSFs of V_{SV} for 20, 80, 140 and 200 km depth are displayed in Figure 5. We present the results of the estimation of the V_{SV}

resolution separately for the two data sets in Supporting Information S1 (Figures S17–S19). We also calculate the PSFs of V_P and V_{SH} only for earthquake data (Figures S20–S22 in Supporting Information S1).

Through the PSF tests for the V_{SV}, we find that earthquake data has less horizontal smearing in the crust and upper mantle down to 260 km than the EGFs, for which there is southwest-northeast smearing in the deep crust and upper mantle. However, in the upper mantle (80–140 km in depth), the Central Tian Shan area is also well illuminated by EGFs. From the PSF comparison between the earthquake waveforms and EGFs, we conclude that the surface waves derived from EGFs are prone to suffer from horizontal smearing. The earthquake FWI utilizes body wave phases and therefore has a better distribution of ray path directions.

Through the multi-parameter point-spread tests, we could confirm that the resolution in the crust is the highest (20–25 km). For the upper mantle, V_{SV}, V_{SH} and V_P could be resolved with 30–40 km spatial resolution down to 250 km in depth, although they suffer from weak smearing and some cross-talks between parameter classes, particularly between V_{SV} and V_{SH} (Figures S17–S22 in Supporting Information S1).

4. Results

Here we present the final 3D seismic velocity model for Central Asia including Pamir, Hindu Kush, West-Central Tian Shan, Tarim, Tajik, and Ferghana Basin. Depth slices of isotropic S wave velocity are shown in Figures 6–9, and cross sections in Figures 10 and 11. Additional cross-sections are displayed in Figures S9 and S10 in Supporting Information S1, results for V_P are shown in Figures S5 and S8 in Supporting Information S1, and radial anisotropy in Figures S11 and S12 in Supporting Information S1. We also provide the velocity image from iteration 48 for comparison (Figures S13–S16 in Supporting Information S1).

We will introduce the major features of the V_S model in the following section. The acronyms used in the figures for geological features and tectonic units are listed in Table A1. The waveform comparisons for both data sets between the observed and synthetic waveforms from the initial and the final model are displayed in Figures S23–S54 in Supporting Information S1.

4.1. Crustal Structure and Moho Depth Estimation

In the shallow crust (10 km, Figure 6a), low-velocity anomalies (down to −25%) are imaged beneath the Tarim, Ferghana and Tajik basins, representing thick sediments. Some deep faults can also be identified and are characterized by low velocities, for example, the low-velocity anomaly in the northwest corner of the Tarim basin extends to 20 km and correlates with the location of a series of faults, consistent with surface wave tomography results (W. Li et al., 2018; Lü et al., 2021) and local earthquake tomography (Bloch et al., 2021).

In the middle to lower crust (20–40 km, Figures 6b–6d), low-velocity zones (LVZ1 and LVZ2, −23% to −20%) mainly follow the curvature of the sutures and main thrust faults beneath the Afghan Pamir (LVZ2) and North Pamir (LVZ1) as well as a part of West Tian Shan. LVZ1 displays its lowest velocity beneath the eastern part of North Pamir, across the whole crust down to 80 km depth (Figure 8). Beneath the Shakhdara-Alichur gneiss dome, West Pamir, a weak low-velocity anomaly (LVZ3, −15%), separate from LVZ2, is detected. A southeast-northwest extending low-velocity zone covers the central part of the Karakorum and Tajik-South Pamir (LVZ4). Isolated from the large-scale Pamir low-velocity anomalies(LVZ1-4), a strong low velocity (LVZ5, −20%) is detected below the Hindu Kush, also consistent with previous studies (Kufner et al., 2021; W. Li et al., 2018). In contrast, beneath the three basins, strong high-velocity anomalies (+21%) indicate the presence of mantle lithosphere (40 km, Figure 6d) and imply a shallow Moho around 30 km. Low velocities (−20% to −10%) still dominate the whole Pamir plateau and West Tian Shan in the 60–80 km depth slices (Figures 8a and 8b), indicating the lowermost thickened crust.

To further estimate crustal thickness, we extract the Moho depth, following the contours of either 4.0 km/s or 4.2 km/s as a proxy for Moho depth (Lu et al., 2020), and compare the result with the Moho maps (Figure 7) from previous receiver function (RF) studies (Schneider et al., 2019; Q. Xu et al., 2021) and Bouguer anomaly maps (Bonvalot et al., 2012). We note that these two contours should be good proxies beneath the basins and the orogenic systems (Lu et al., 2020; Nouibat et al., 2023) but could fail to represent the Moho depth in areas of strong structural variation, for example, where subduction occurs. The strong low Bouguer anomaly occupies the whole central part of Pamir and extends to the West-Central Tian Shan and Hindu Kush, confirming the large-scale thick crust inferred from previous studies (ranging from 60 to 80 km). Along the west and east flanks of

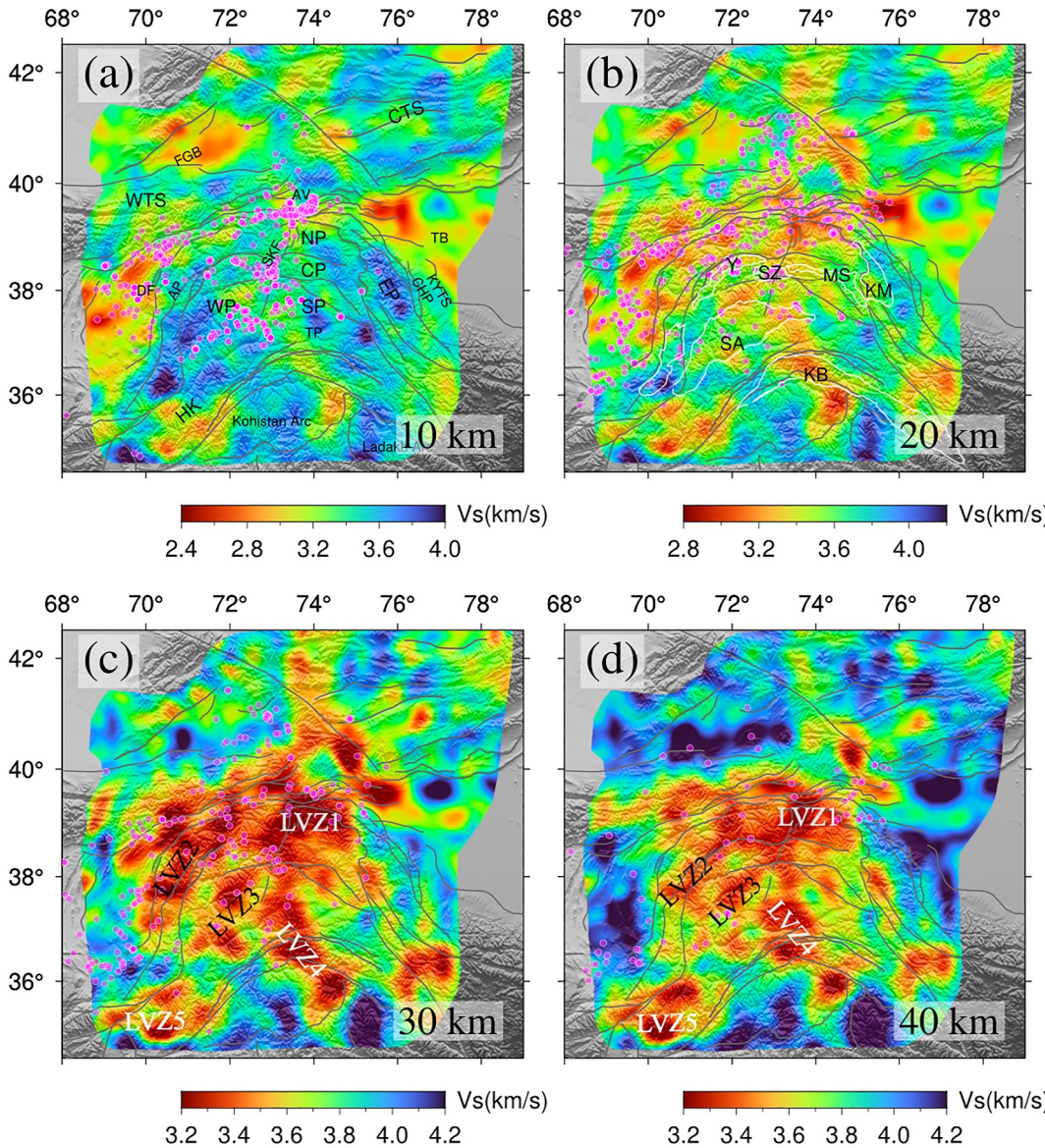

Figure 6. Horizontal slices of the isotropic $\mathbf{V}_S$ in the crust: four panels denote the isotropic $\mathbf{V}_S$ in the crust. The magenta circles denote the crustal seismicity retrieved from the previous study (Kufner, Schurr, et al., 2018) with 5 km interval in depth.

the Pamir and most of the North Pamir, we image a Moho as deep as 80 km (Figure 7), in agreement with previous RF studies (Schneider et al., 2019; Q. Xu et al., 2021). In the eastern part of the Central Pamir, a relatively shallower Moho (60 km) is obtained, which is separated by the Sarez-Karakul Fault System from the western deep Moho (70–80 km). In contrast, beneath the basins, the Moho is shallow (30–50 km) and generally consistent with RF studies (Schneider et al., 2019; Q. Xu et al., 2021). In addition, we detect a deepened Moho beneath the Hindu Kush (over 90 km) (Acosta et al., 2023), Tajik Pamir (70–80 km) and West Tian Shan (70–80 km). The Hindu Kush involves marginal Indian plate subduction, indicating prominent velocity perturbation and involving complicated crustal-mantle material exchange. We extend our analysis and interpretation in the next section. The Tajik Pamir has potentially experienced cratonic Indian plate indentation, indicating past crustal thickening and shortening (Kumar et al., 2022; Sass et al., 2014; Schneider et al., 2019). The West Tian displays a single and narrow deep Moho along the orogeny. For the Central Tian Shan, the Moho depth varies significantly with latitude. At the north and south edges of Central Tian Shan, a very deep Moho down to 70–80 km is observed while the middle part of the Central Tian Shan exhibits a relatively shallower Moho (50–60 km, Figure 7),

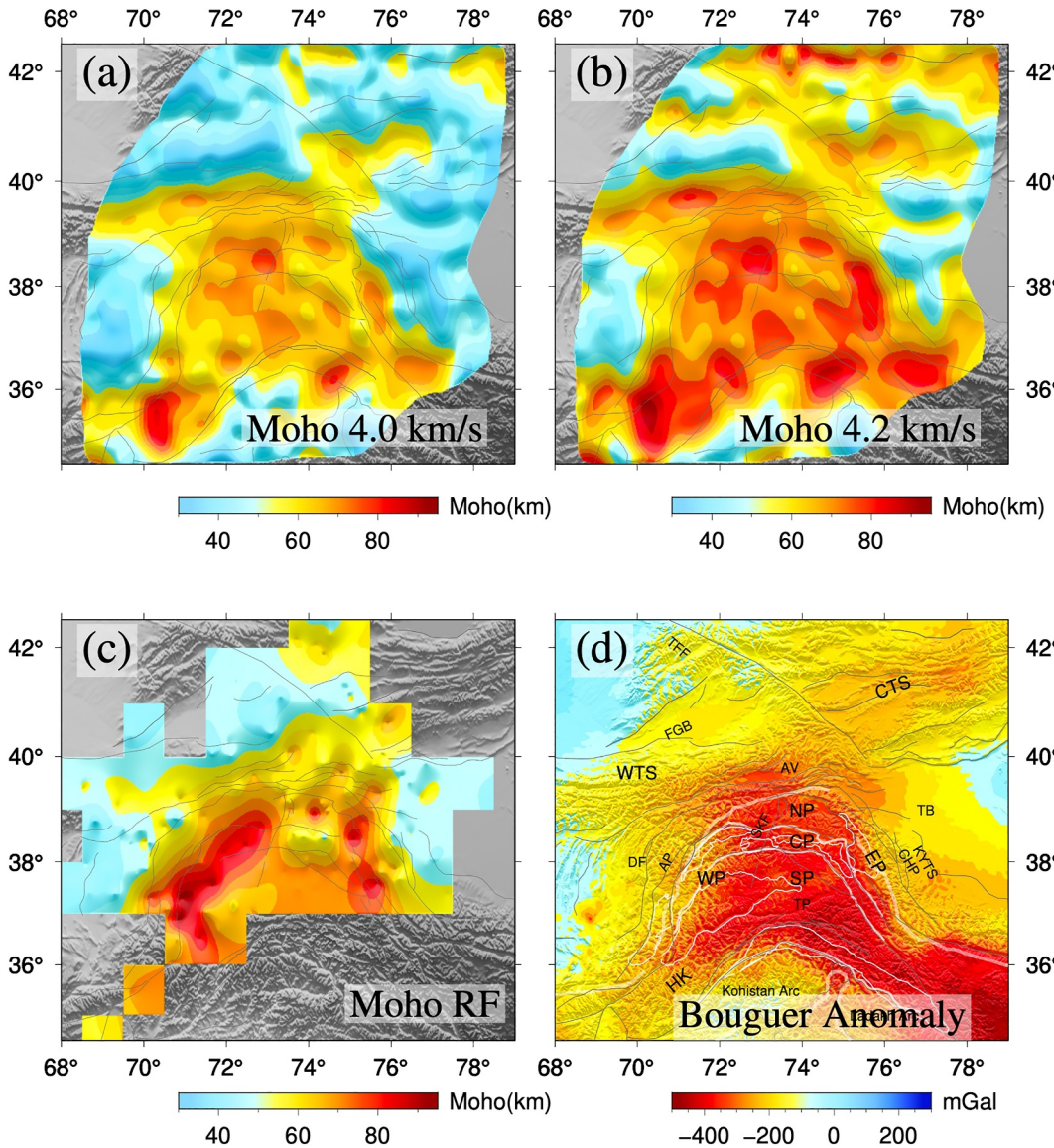

Figure 7. (a–b) Moho depth estimate using either 4.0 km/s (a) and 4.2 km/s (b) $\mathbf{V}_S$ contours as proxy. (c) Moho depth from previous receiver function studies (Schneider et al., 2019; Q. Xu et al., 2021). (d) Bouguer Anomaly from Bonvalot et al. (2012).

indicating a complicated sandwich thrust and orogeny structure (Huang et al., 2016; W. Li et al., 2022; Lü et al., 2020; Zhang et al., 2020).

The Moho depth map (4.2 km/s) retrieved from the S wave velocity model agrees even better with previous receiver function studies (Schneider et al., 2019; Q. Xu et al., 2021) than 4.0 km/s, not only in terms of variation patterns but also absolute Moho depth. The newly estimated Moho depth based on this study provides a more comprehensive Moho map for the whole western syntaxis of the India-Asia collision system.

4.2. Upper Mantle Structure

In the uppermost mantle (60–80 km, Figure 8), high-velocity anomalies (with S wave velocity ranging from 4.5 to 4.8 km/s, up to +7%) are imaged beneath the Tarim, Tajik, and Ferghana Basins, similar to the typical cratonic velocities in the uppermost mantle of North America (e.g., H. Yuan et al., 2011). The high velocity and thin crust (Figure 7) indicate a strong and stable cratonic lithosphere (Schneider et al., 2019; Xiao et al., 2010).

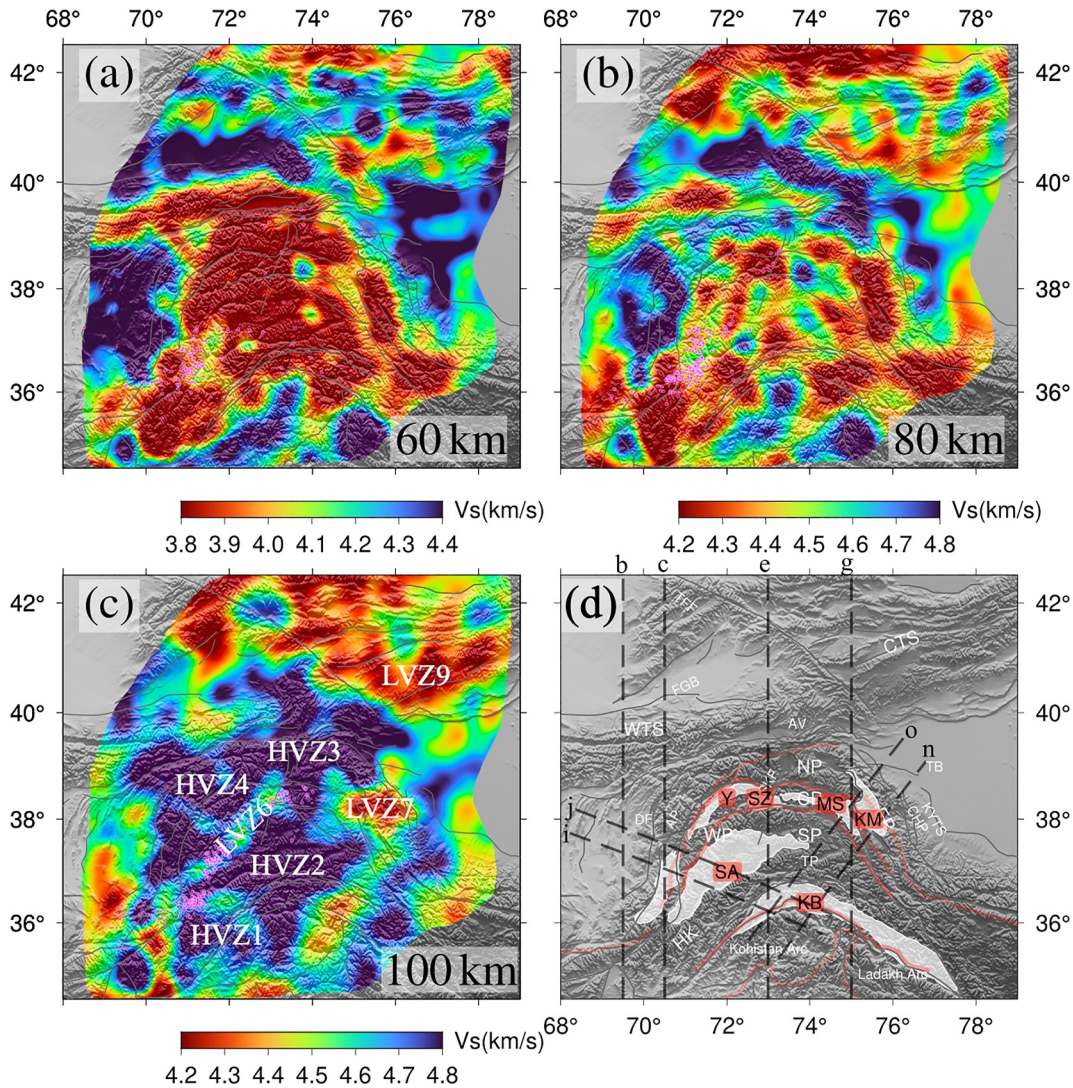

Figure 8. (a–c) Horizontal slices of isotropic V_S in the lower crust and uppermost mantle from 60 to 100 km. (d) Displays the profile locations in Figures 10 and 11. More cross-section profiles and model images are illustrated in Figures S9 and S10 in Supporting Information S1. For the explanation of acronyms, see Table A1 and the caption of Figure 2. The magenta circles denote the intermediate depth seismicity retrieved from previous studies (Bloch et al., 2021; Kufner et al., 2017; Sippl et al., 2013) with 5 km interval in depth.

In contrast, the whole Pamir, Hindu Kush and West Tian Shan have a 60–80 km thick crust with low velocities (Figures 8, 10, and 11). The low-velocity anomalies (−7%) penetrate deeper into the uppermost mantle, along the Afghan and Chinese Pamir and part of the Tajik Pamir. Unlike the West Tian Shan, the Central Tian Shan (Figure 8) displays a more heterogeneous mantle structure, with the central part demonstrating normal to high velocities in this depth range, while the south and north edges display low velocities (W. Li et al., 2022), correlating with the variational topography of the Moho. We note that the Hindu Kush shows an even stronger and deeper low-velocity anomaly than the Pamir at 100–120 km depth, which is then hard to attribute to a depressed Moho or felsic composition of the lower crust alone but rather is likely to be related to subduction of the lower crust and/or the presence of higher temperatures or fluid concentration (Kufner et al., 2016, 2021), we will expand our discussion in the next section.

In the upper mantle (100–120 km), the South-Tajik Pamir is underlain by a large and strong high-velocity anomaly (HVZ2, +6% in Figures 8–11), which is separated by a narrow weak low-velocity zone (LVZ6, −2%) from the curved high-velocity anomalies (HVZ3 and HVZ4, +7%), beneath the Afghan and North Pamir

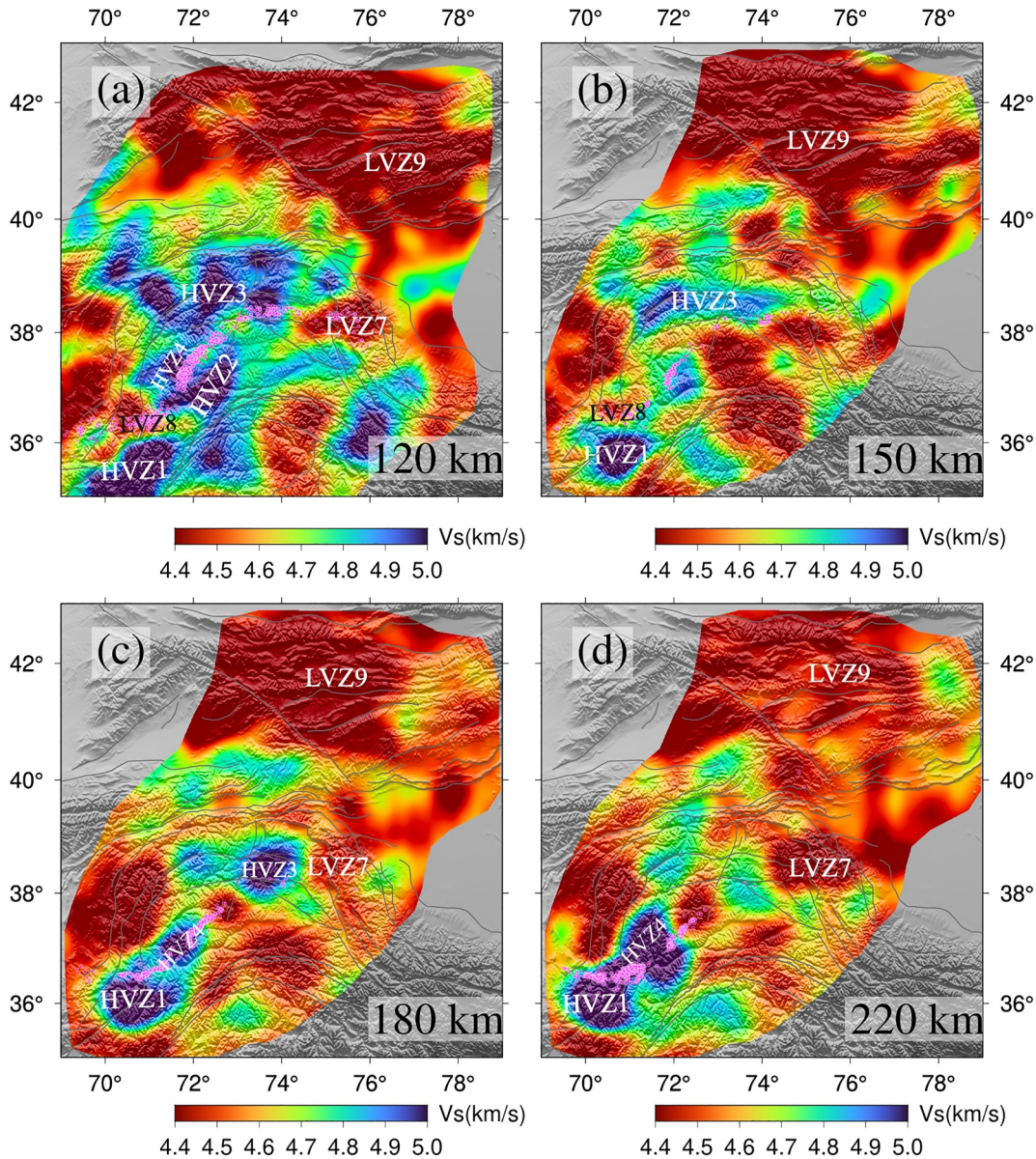

Figure 9. Horizontal slices in the upper mantle from 120 to 220 km. The magenta circles denote the intermediate-depth seismicity retrieved from previous studies (Bloch et al., 2021; Kufner et al., 2017; Sippl et al., 2013) with 5 km interval in depth.

(Sippl et al., 2013; W. Li et al., 2018; Liang et al., 2020; Kumar et al., 2022); LVZ6 coincides with intermediate-depth seismicity (Bloch et al., 2021; Kufner et al., 2016). The northeast corner of HVZ2 is separated by another strong low-velocity anomaly LVZ7 (−7%) from the Tarim Basin.

The Central Tian Shan is underlain by a large low-velocity anomaly (LVZ9, −6%), which extends from 100 to 220 km depth, similar to previous tomography studies (Y. Xu et al., 2007; Z. Li et al., 2009; Gilligan et al., 2014; W. Li et al., 2022) and is separated by the Talas-Ferghana fault from the Ferghana Basin and the northwest tip of the Tarim Basin. Meanwhile, beneath the eastern Tajik Basin, small-scale low-velocity anomalies are observed to the northwest of the Hindu Kush and Afghan Pamir (Kufner et al., 2021), possibly indicating the presence of asthenosphere at these depths.

In the deeper upper mantle beneath the Hindu Kush and Afghan, West and North Pamir, we can still observe high-velocity anomalies with HVZ3 down to 180–200 km and HVZ1 (+7 to +8%) and HVZ4 down to >220 km,

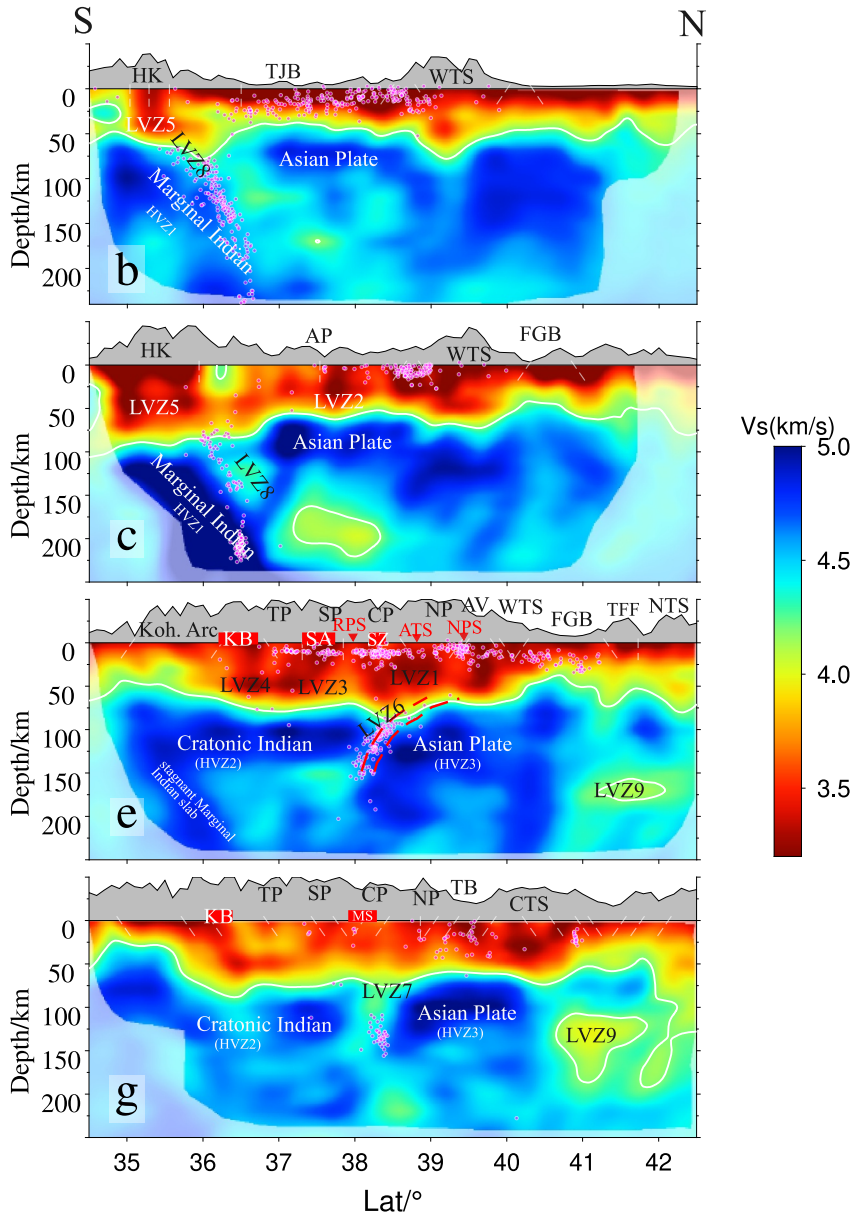

Figure 10. Four vertical south-north cross-sections from west to east. The position of cross-sections is indicated in Figure 8. The magenta circles denote the seismicity (swath width 25 km) retrieved from previous studies including (Bloch et al., 2021; Kufner et al., 2016, 2017). The short white dashed lines in the crust denote the position and dip direction of the tectonic faults (Mohadjer et al., 2016). The red bars on the surface mark the position of Cenozoic gneiss domes (Schneider et al., 2019). The red dashed lines in Profile e denote the position of the delaminated lower crust derived from receiver function studies (Schneider et al., 2013).

hinting at a subduction or delamination environment involving lithospheric material dripping or subducting. HVZ1 also seems to extend eastward beneath the Kohistan Arc region with depth down until 220 km where it becomes weaker. In cross-sections b and c (Figure 10) beneath the Hindu Kush, the high-velocity anomaly (HVZ1) steeply dips northward down to ~180 km, then becoming nearly vertical below 200 km and reaching the bottom of the resolved region, consistent with previous teleseismic tomography results (Koulakov & Sobolev, 2006; Kufner et al., 2016, 2021), which imaged high velocities extending down to 400–600 km. HVZ1 can be traced further east along the cross-section profile e (Figure 10), but, it is no longer accompanied by intermediate-depth seismicity there.

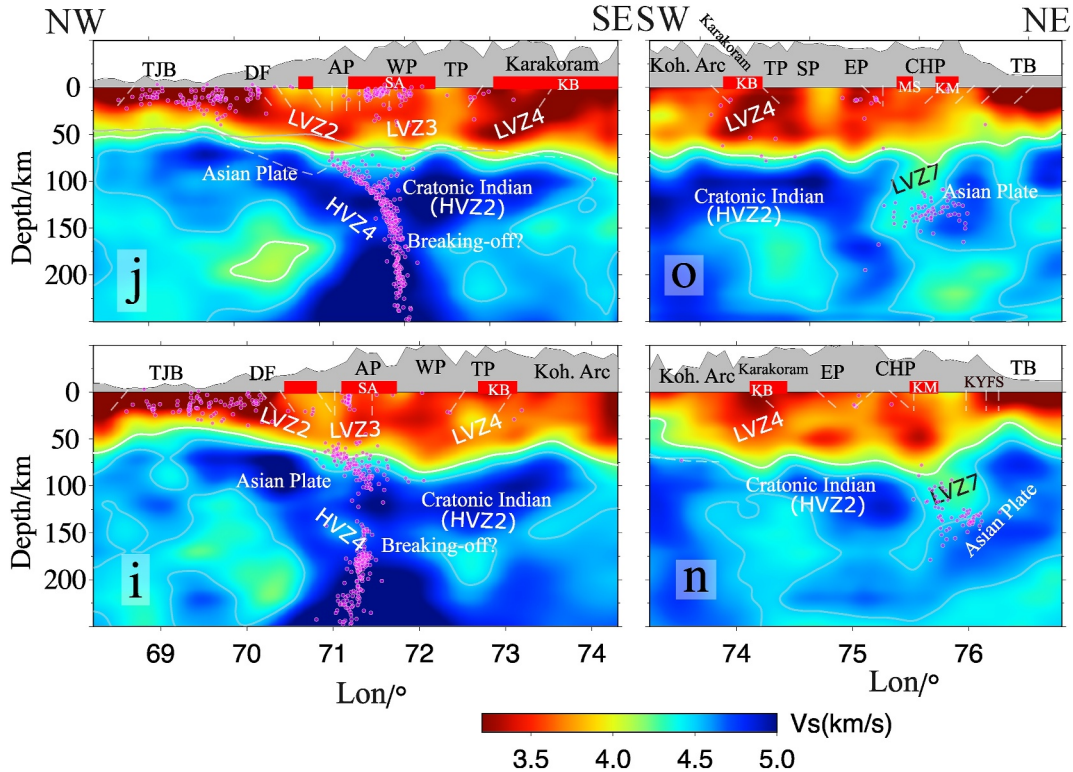

Figure 11. Four oblique cross-sections across the boundaries of the Tajik basin and West Pamir (i–j), Tarim basin and East Pamir (o–n). The position of cross-sections is indicated in Figure 8d. Other elements are the same as Figure 10.

Beneath the Afghan and West Pamir (cross-section i-j, Figure 11), the high-velocity anomaly HVZ4 seems only weakly connected or even separate from two high-velocity anomalies that correspond to the lithosphere beneath the Tajik Basin and the large-scale high velocity (HVZ2) beneath the Tajik Pamir and Karakorum. In contrast, beneath the northern and Central Pamir (cross-section e in Figure 10), the upper mantle's high velocity (HVZ3) dips southward down to 200 km depth with intense seismicity and a low-velocity layer (LVZ6) at the top.

5. Discussion

5.1. Subduction of the Marginal Indian Slab Beneath the Hindu Kush

A subduction setting for the Hindu Kush has been proposed and documented by previous studies (Burtman & Molnar, 1993; Kufner et al., 2016, 2021) but is also challenged by an alternative interpretation involving lithospheric foundering from the Asian side, such as sinking and stretching of thickened Asian mantle lithosphere beneath the Hindu Kush (Molnar & Bendick, 2019; Perry et al., 2019). The subduction interpretation (Kufner et al., 2021; W. Li et al., 2018) argues that the marginal Indian slab is subducting beneath the Hindu Kush, deepening eastwards and even breaking off at a depth of 200–300 km beneath the western Hindu Kush, to over 600 km beneath the central Hindu Kush (e.g., Kufner et al., 2016, 2017, 2021). Beneath the Hindu Kush (Profiles b and c in Figure 10), we image a northward dipping high-velocity anomaly (HVZ1) in the upper mantle, which could further support and confirm the subduction environment, that the subducting marginal Indian plate is subducting northwards beneath Hindu Kush and Tajik Basin. A low-velocity layer (LVZ8) is attached on the top of the subducting Indian slab (HVZ1), parallel to the steeply subducting mantle lithosphere; this layer hosts most of the intermediate-depth seismicity at 100–150 km depth (Profile c in Figure 10). This structure possibly represents the lower crust of the marginal Indian plate (Kufner et al., 2021), indicating lower crust subduction and strong coupling between the lower crust and mantle lithosphere. Metamorphic dehydration reactions within the subducted lower crust may reduce the effective pressure and thus enable intermediate-depth seismicity through dehydration embrittlement effects (Hacker et al., 2003), for example, along pre-existing weakness zones such as fossil faults.

In the overriding plate beneath the Hindu Kush, extensive low-velocity anomalies in the lower crust may indicate melting in the overthickened crust (up to 90 km thick). The dehydration effects of the subducting crust may provide an additional source of fluids that migrate into the lower crust of the overriding plate and lower the melting point there. Melt production might be further promoted by rapid exhumation of previously delaminated crust, which would be a mechanism to add heat energy to the crust via advection, as proposed by Kufner et al. (2021).

Deeper seismicity at depths larger than 200 km is mainly located within the lithospheric slab mantle. It is triggered by the hyper-extension of the slab caused by the loss of slab buoyancy following eclogitization in the subducting crust (Kufner et al., 2017, 2021). Note that from profile (b) to (c), there is a change of the overriding plate from the relatively flat and rigid Asian lithosphere beneath the Tajik basin to the highly deformed Asian lithosphere (HVZ4) beneath the Afghan Pamir where the Asian plate is believed to be delaminated beneath the Central and West Pamir (Schneider et al., 2019; Sippl et al., 2013); therefore we observe a shallow Moho beneath the Tajik Basin along profile (b), while a deep Moho and southeastward dipping lithosphere are seen in profile c.

The steeply subducting Indian slab beneath the Hindu Kush can be traced eastward beneath the Kohistan Arc to the south of Pamir in our model (Figure 10). Kufner et al. (2017) proposed a break-off in the subducted Indian slab at a depth of about 180 km that started from the eastern Hindu Kush and propagated westwards. The involvement of the lower crust in the subducted slab adds buoyancy to the upper portion of the slab, causing slab shearing, necking, and break-off. While this process is still ongoing beneath the Hindu Kush, the deeper slab portion probably has already detached beneath the Kohistan Arc, leaving the upper slab portion hanging in the mantle. This slab segment was overridden by the continuously northward advancing cratonic Indian lithosphere (HVZ2). Due to buoyancy, this remnant slab segment remains neutrally buoyant in the upper mantle without being recycled into the deep mantle. It is not associated with any earthquake activity. However, due to the data coverage limitations, this interpretation remains tentative until more extended station coverage can be implemented for south of 36° N in the Kohistan Arc.

5.2. Indentation of Cratonic Indian Lithosphere

Beneath the Pamir, the marginal India slab has detached from the cratonic Indian lithosphere (Kufner et al., 2016; Sippl et al., 2013). The cratonic Indian plate continues to move northward and indents into the South and Central Pamir, forcing Asian plate delamination and rollback (Kufner et al., 2016; Schneider et al., 2019; Q. Xu et al., 2021), leading to an arc shape deep Moho trough. Due to data coverage limitation, most previous studies only revealed the low-velocity zone in the uppermost mantle along the intermediate-depth seismicity (W. Li et al., 2018; Liang et al., 2020; Sippl et al., 2013). The cratonic Indian plate beneath the Pamir has not been imaged clearly in these studies even though recent large-scale surface wave tomography (Kumar et al., 2022; Liang et al., 2020) captured some clues about the indented Indian plate beneath South Pamir and Tajik Pamir at 100 km depth. At the same depth (Figure 8), our model depicts a promontory-shaped high-velocity anomaly (HVZ2) with its northern boundary meeting the curved intermediate-depth seismicity zone extending from the West-Afghan Pamir to the central and East-Chinese Pamir. We interpret this feature as the cratonic Indian plate, agreeing with the predicted location from numerical modeling results (Liao et al., 2017). In depth, the cratonic Indian plate is flat, very distinct from the steep marginal Indian slab beneath the Hindu Kush. Along Profile e in Figure 10, the cratonic Indian plate meets the Asian plate beneath the Central Pamir at 38–39°N. The thickness of the flat Cratonic Indian plate lithosphere is around 50–75 km with an S wave velocity of 4.5–4.8 km/s, which is in the range of shear wave velocity values of typical cratonic lithosphere (H. Yuan et al., 2011).

The direct observation and discovery of the indented and promontory-shaped cratonic Indian plate lithosphere beneath Pamir serve to confirm several previous interpretations about the location of the cratonic Indian plate and reason for the delamination of the Asian plate (e.g., Burtman & Molnar, 1993; Kufner et al., 2017; Sippl et al., 2013), which could further explain the over-thickened crust (Schneider et al., 2019), the development of arc-shape amalgamation and strike-slip faults along the west and east flanks of the Pamir (Schurr et al., 2014). The position and shape of the indented cratonic Indian plate in relation to subducted slabs are further illustrated in the conception model shown in Figure 12. In the following subsections, we will expand our interpretation and discussion of the tomographic model in the contact zone within the crust and uppermost mantle along the collision front of the cratonic Indian and original Asian lithosphere including the Tajik-Tarim basins and amalgamation terranes in the Pamir.

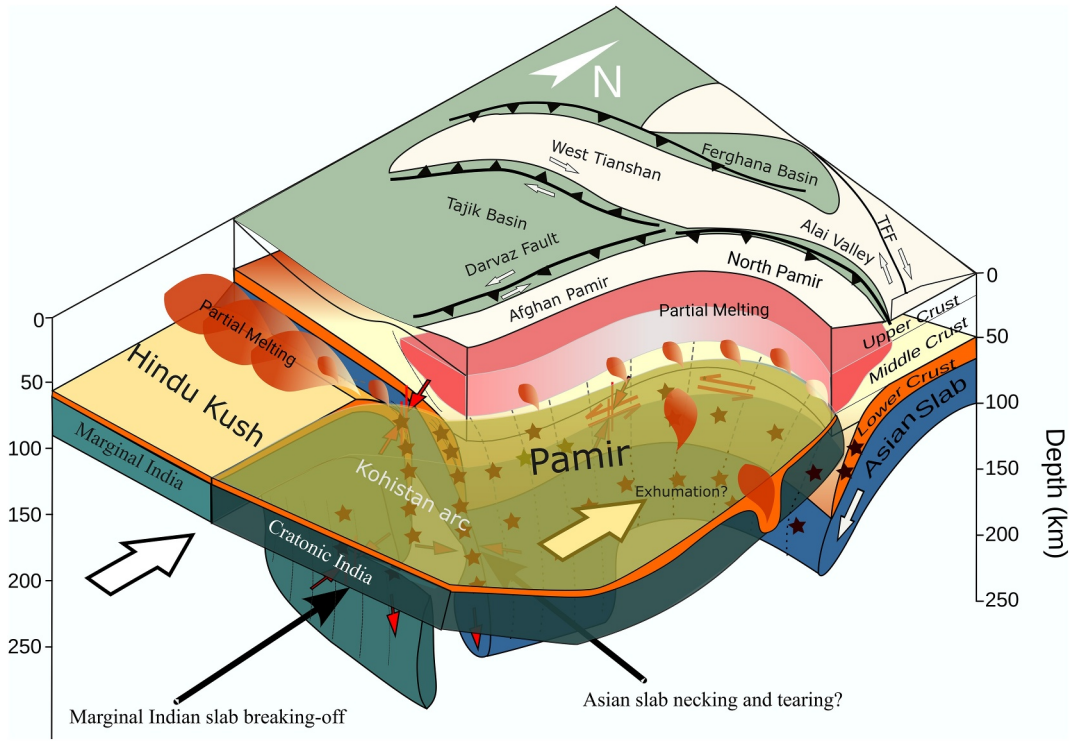

Figure 12. Geodynamic process cartoon for Pamir and the Hindu Kush, modified from W. Li et al. (2018). In the west (left), marginal India is underthrusting the Tajik basin, and then subducting steeply below the Hindu Kush. At 150–180 km depth this slab is undergoing breakoff. An older slab, which has detached previously, can be seen further east below the Kohistan Arc. To the east of the Marginal Indian slab, the cratonic Indian plate acts as a rigid indenter of the Pamir. This process triggers delamination of the lower crust and mantle lithosphere from the Asian plate, leading to the presence of a continuous slab down to 120–150 km. Here, the delaminating Asian slab beneath the West Pamir extends deeper than the North Pamir. Below this depth, lower curst material can be expected to eclogitize, meaning it will no longer be visible in the mode or generate earthquakes, but the crustal slivers might remain.

5.2.1. Intense Delamination of the Asian Lower Crust and Lithosphere, Fluid Migration, and Accumulation

The profile along 73°E (Profile e in Figure 10) depicts the direct collision scenario between the Indian craton with the Asian plate beneath the Central Pamir, parallel to the NNW convergence direction. The collision has previously been explored through travel time tomography (W. Li et al., 2020; Sippl et al., 2013), receiver functions (W. Li et al., 2020; Schneider et al., 2013), and guided wave modeling (Mechie et al., 2019), which revealed a south-dipping low-velocity zone with a thickness of around 10–15 km, interpreted as the Asian delaminated (subducting) lower crust. In this study, the thin delaminated lower crust is recovered as a low-velocity layer (LVZ6) attached to the southward delaminating high-velocity Asian plate lithosphere (HVZ3) beneath the Central Pamir. The very deep Moho to 80 km (Figure 7) beneath the Central Pamir is highly consistent with receiver function studies (Schneider et al., 2013, 2019), which discovered a double Moho beneath the Central Pamir. The southward dipping Moho (lower red dashed line in Figure 10e) due to the delamination of the lower crust agrees very well with the bottom of the low-velocity delaminated lower crust (LVZ6) in our model.

The delaminating lower crust from the Asian plate follows the intermediate-depth seismicity down to 150 km. The lower crust is then indistinguishable from the asthenosphere beneath the indenting lithosphere of the Indian carton (HVZ2). The disappearance of intermediate-depth seismicity deeper than 150 km indicates that metamorphic reactions terminate within the lower crust before it submerses into the deeper mantle. With metamorphic reactions within the delaminating lower crust of the Asian plate will release some metamorphic fluids (W. Li et al., 2020; Sippl et al., 2013), which will migrate upwards and accumulate within the overridden middle-lower crust of the Central-North Pamir. Fluids possibly further facilitate the crustal partial melting causing prominent low velocities (LVZ1) in the middle-lower crust (Profile e in Figure 10; Figures 6c and 6d). These low-velocity

anomalies in the middle-lower crust correlate with the existence of high conductivity zones from magnetotelluric experiments (Sass et al., 2014). The low-velocity anomaly is also consistent with the position of suture zones including Rushan–Pshart Suture and Akbaytal–Tanymas Suture, which separates the Pamir into South, Central, and North Pamir, respectively, and represents weak zones with brittle deformation with vigorous crustal seismicity (Figure 6c). Meanwhile, the delamination of the Asian lithosphere possibly drove the overlying Pamir crust from a compressional state into an extensional regime, facilitating the exhumation of metamorphic rocks in a series of Pamir gneiss domes (Tang et al., 2024; Worthington et al., 2020), such as the Sarez gneiss dome.

Above the flat Indian plate (HVZ2), the lower crust also displays low-velocity features (LVZ3, 4) extending from South Pamir to the Karakorum, consistent with the location of the Shakhdara-Alichur dome and Karakoram Batholith (Profile e in Figure 10). Sass et al. (2014) detected very high electrical conductivities in the middle-lower crust beneath the South Pamir, representing the crustal partial molten rocks beneath these gneiss domes and batholith (Schneider et al., 2019).

5.2.2. Westward Pamir Crust Extrusion and Tajik Basin Lithosphere Delamination

The Tajik Basin is covered by thick low-velocity sediments up to 10 km (Chapman et al., 2020) and a normal crust (around 40 km) is imaged by receiver function (Schneider et al., 2019), local tomography (Kufner et al., 2017; Sippl et al., 2013) and this study (Figure 6; Profile b in Figure 10 and Profile i-j in Figure 11). The mantle lithosphere beneath the Tajik Basin extends from the shallow Moho down to around 100 km depth. At the base of the sediments (10 km), intense seismicity (Kufner, Schurr, et al., 2018) is detected and dips progressively southeastward within a low-velocity layer until it intersects the Moho (Profile i in Figures 7 and 11). The seismicity pattern has been documented by regional seismotectonic studies (Kufner, Schurr, et al., 2018; Schurr et al., 2014), which explain west-east sub-horizontally orientated thrust focal mechanisms in this area as a horizontal slip of the sediments over the basal décollement, marked by the Jurassic evaporite layer.

In this study, the northern and eastern margins of the Tajik Basin are first characterized by low velocities in the upper-middle crust with a shallow Moho. Transitions to a thick crust and low velocities in the lower crust occur on the edges of the Tajik basin: the West Tian Shan in the north (Profile b in Figure 10) and Afghan Pamir in the southeast (in Profile i in Figure 11). The latter transition is marked by the east-dipping sinistral Darvaz fault, which delineates the boundary between the Tajik Basin and Afghan Pamir. These structures form a southeast dipping crustal low-velocity ramp (LVZ2) from the Tajik Basin to the Afghan-West Pamir. The clear low-velocity ramp revealed in this study is also accompanied by intense seismicity, which shows a dominant thrust component (Kufner, Schurr, et al., 2018).

Similar to the structure beneath the northern Central Pamir along Profile (e), where the lithosphere and lower crust of the Asian Plate delaminates, we detect a southeast dipping high-velocity structure (HVZ4) beneath the Afghan and West Pamir correlating with dipping intermediate-depth seismicity along Profile i and j in Figure 11. We confirm that with the northward indentation of the Cratonic Indian lithosphere, the sinistral Darvaz fault accommodates the large-scale northward movement of the Pamir crust relative to the rigid Tajik Basin (Ge et al., 2022). Meanwhile, the upper crustal material collapses and extrudes westwards across the Darvaz fault and a series of east-dipping thrust faults. The sedimentary stack of the Tajik basin along with upper-middle crust material is underthrusted as the footwall of this fault zone. Buoyant upper-middle crust material is then accumulated beneath the West-Afghan Pamir, causing the formation of the thickest crust in this region and contributing to the formation of the Shakhdara-Alichur dome with the delamination of the Asian plate from the Tajik Basin.

In addition, the south-east delaminated Asian plate (HVZ4) from the Tajik Basin seems to be thinned at a depth of 150 km, forming a necking feature (Profile i and j in Figure 11), potentially indicating a tearing or breaking-off process of the delaminating slab due to the negative buoyancy (More cross-sections could be found in Figure S10 in Supporting Information S1). As continuous northward indentation, the cratonic Indian plate is driving the delamination of the Asian plate, the lower crust is pushed to the deep where it undergoes eclogitization, such that the buoyancy drops and the necking of the slab is triggered (Figure 12).

5.2.3. Underthrusting of Pamir Lower Crust and Delamination of Tarim Basin Lithosphere

Beneath the Chinese Pamir, a thick and strong low-velocity anomaly (LVZ7) penetrates from the lower crust down to 150 km, forming the top boundary of an intermediate-seismicity cluster (Profile o in Figure 11). We can

clearly distinguish the Indian plate from the Asian plate beneath the Tarim Basin. Receiver function studies reveal a Moho doublet, which is interpreted as underthrusting of the lower crust from the South and East-Chinese Pamir (Q. Xu et al., 2021; Bloch et al., 2021), which spatially correlates well with the low velocity from our model. Meanwhile, the exhumation of delaminated crust from the Asian plate or Pamir crust may also occur and cause the formation of gneiss domes including the Muskol-Shatput dome and the Kongur Shan-Muztaghata dome. These high-grade gneiss domes are formed by large-scale crustal extension with exhumation from 30 to 50 km depth (Hacker et al., 2017; Schneider et al., 2019). Interestingly, beneath the Muskol-Shatput dome, erupted xenoliths were also found, indicating a rapid thickening and foundering of the Pamir lithosphere at 14–11 Ma, before and synchronous with the collision between Indian and Asian lithospheres beneath the Pamir (Shaffer et al., 2017). Our model probably captured a channel (LVZ7) composed of foundering crustal material, which might include fragments of Indian plate affinity from the southwest and Asian plate affinity from the east, causing a localized Moho depression and exhumation of the foundering crust with partial melts, supported by the erupted xenoliths in the Chinese Pamir (Shaffer et al., 2017).

The lithosphere from the Tarim Basin seems to be southwest dipping, extending from the base of the Tarim Basin down to 150 km beneath the Chinese Pamir. We infer that the delamination of part of the Asian lithosphere from the Tarim Basin is ongoing beneath the transition between the East-Chinese Pamir and the northwest tip of the Tarim. Due to the data coverage within the Tarim basin, the resolution for the East Pamir is worse than the Northern and West Pamir, so we will not discuss these structures further.

5.3. Contrasting Lithosphere Structure of the Western and Central Tian Shan

The model in this study showed significant differences in the seismic structure of the crust and upper mantle between the West and Central Tian Shan. The crust features a low-velocity zone and a deep Moho, forming a narrow Moho trough (Figures 6 and 7) beneath the West Tian Shan (Schneider et al., 2019). In contrast, the crust of the Central Tian Shan exhibits high velocities except for the weak low-velocity anomaly within the upper crust along the Talas Ferghana fault, indicating the deep penetration of this fault (Figure 6b). The Moho beneath the Central Tian Shan is more complicated than the West Tian Shan. The north and south parts of Central Tian Shan are characterized by a deep Moho of 80 km whereas the Moho in the central part is shallower (50 km). The shallower Moho (Gilligan et al., 2014) is underlain by a small-scale high-velocity mantle lid at a depth of 50–100 km just beneath the low-topographic middle Central Tian Shan (Profile g in Figure 10). Beneath this weak high-velocity lid we interpret the large-scale low-velocity (LVZ9) as asthenosphere.

Several receiver function studies (W. Li et al., 2022; Lü et al., 2020; Zhang et al., 2020) depicted a roughly similar Moho pattern. Lü et al. (2019, 2021) directly attributed the LVZ9 in the uppermost mantle beneath the Central Tian Shan to the upwelling of a mantle plume but ignored the existence of the lithosphere lid in the middle of the Central Tian Shan (Gilligan et al., 2014; W. Li et al., 2022). This thin lithospheric lid is accompanied by a deep Moho and thrust faults on both sides which provides evidence for underthrusting of the Tarim Basin block beneath the southern margin of the Central Tian Shan (Huang et al., 2016) and the Kazakh shield beneath the northern margin (Z. Li et al., 2009; W. Li et al., 2022). The lithosphere beneath the middle Central Tian Shan might be partially delaminated and broken compared to the Tarim Basin, which is rather stable. In contrast, the West Tian Shan orogeny, rather narrow, is sandwiched by the Tajik Basin, Pamir Plateau and Ferghana Basin, to the south and north, respectively.

6. Conclusion

In this study, we employed joint full waveform inversion based on earthquakes and empirical Greens' functions extracted from ambient noise to image the seismic velocity structure in the crust and upper mantle beneath Central Asia including the Hindu Kush, Pamir, and West and Central Tian Shan. We discussed the $\mathbf{V}_S$ model, which has the best resolution but also inverted for and presented the P wave and radial anisotropic S wave velocity models. The new velocity model provides a more comprehensive understanding of the current configuration among the marginal Indian and cratonic Indian plates, the Asian plate beneath the Pamir, the Tian Shan, and the cratonic Asian plate beneath the cratonic basins.

We analyze the interactions among adjacent tectonic units based on our seismic model. Many of our conclusions are summarized in Figure 12.

1. Beneath the Hindu Kush, our model clearly images the marginal Indian lithosphere subducting steeply northwards beneath the Hindu Kush and Tajik Basin. The subduction of the lower crust attached to the marginal Indian lithosphere causes metamorphic reactions, providing a source of heating and fluids for the melting of the lower crust of the overriding plate; parts of the crust appear to be exhumed later. An older part of the Marginal Indian slab probably extends below the Kohistan Arc after breaking off from the upper portion of the slab.
2. This study provides a first clear image of the indenting cratonic Indian plate promontory beneath the Pamir as a flat high-velocity anomaly. As a response, the lithosphere and the lower crust of the Asian plate beneath the North and Central Pamir are delaminating southwards beneath the cratonic Indian plate, causing the deepest Moho of Earth. This process is likely driven by the Indian craton acting as a rigid indenter in the collision with the Asian terranes.
3. Due to the indentation of the cratonic Indian plate, we imaged the lower Asian crust being underthrusting beneath the Afghan-West Pamir together with the delamination lithosphere of the Asian mantle lithosphere, forming a continuous curved slab, which is potentially thinned and even breaking off in the deep upper mantle.
4. Along the boundary between the Tarim Basin and East Pamir boundary, a thicker low-velocity layer is imaged in the uppermost mantle and possibly indicates a multiple stacking of crust from the Pamir, Asian plate, and Indian plate, forming a channel of crustal exhumation and partial melts and causing gneiss domes and eruption of xenoliths.
5. The West and Central Tian Shan display significantly different lithosphere structures: the lithosphere beneath the Central Tian Shan possibly has suffered from large-scale destruction with some remnant lid left. The West Tian Shan has a deep Moho due to strong shortening induced by squeezing from the Tajik Basin and Ferghana Basin.

Appendix A: Table of Acronym

The detailed definitions of all geographic acronyms and methodological acronyms mentioned in the figures and main context are listed below.

Table A1
Definitions of All Geographic and Methodological Acronyms

Acronym	Explanation	Acronym	Explanation
AP	Afghan Pamir	*NPS*	North Pamir/Kunlun Suture
ATS	Akbaytal–Tanymas Suture	*NP*	North Pamir
AV	Alai Valley	*RPS*	Rushan–Pshart Suture
CHP	Chinese Pamir	*SA*	Shakhdara-Alichur dome
CP	Central Pamir	*SKF*	Sarez-Karakul Fault System
CTS	Central Tian Shan	*SP*	South Pamir
DF	Darvaz Fault	*SS*	Shyok Suture
EP	East Pamir	*SZ*	Sarez dome
FGB	Ferghana Basin	*TB*	Tarim Basin
HK	Hindu Kush	*TFF*	Talas-Ferghana Fault
IYS	Indus-Yarlung suture	*TJB*	Tajik Basin
KB	Karakoram Batholith	*TP*	Tajik Pamir
KF	Karakorum Fault	*WP*	West Pamir
KM	Kongur Shan-Muztaghata dome	*WKL*	West Kunlun
KYTS	Kashgar-Yecheng Fault System	*WTS*	West Tian Shan
MPT	Main Pamir Thrust	*Y*	Yazgulom dome
MS	Muskol-Shatput dome	*MT*	Muji-Tashkorgan Graben System
FWI	Full waveform inversion	*EPS*	Exponentiated Phase Shift
CCC	Cross Correlation Coefficient	*IPS*	Instaneous Phase Shift
EGFs	Empirical Greens' Functions	*TFPS*	Time-Frequency Phase Shift

Data Availability Statement

Waveform data and station meta-data were downloaded using the ObsPy (Krischer et al., 2015) module through the International Federation of Digital Seismograph Networks (FDSN) web services and obtained from the GEOFON data centre of the GFZ German Research Centre for Geosciences and EarthScope Consortium Data Services. Networks used in this study are listed in Supporting Information S1 (Table S1) including 4C 2017–2019 (Kufner, Kakar, et al., 2018), 5C 2012–2014 (Schurr et al., 2012), 6C 2009–2010 (Haberland et al., 2009), 6C 2013–2014 (Schurr et al., 2013), 7B 2008–2010 (X. Yuan et al., 2008), 8H 2015–2017 (X. Yuan et al., 2017), 9H 2016–2017 (Schurr et al., 2017), CB (Institute of Geophysics China Earthquake Administration (IGPCEA), 2000), G (Institut de physique du globe de Paris (IPGP) & École et Observatoire des Sciences de la Terre de Strasbourg (EOST), 1982), GE (GEOFON Data Centre, 1993), IU (Albuquerque Seismological Laboratory (ASL)/USGS, 1988), II (Scripps Institution of Oceanography, 1986), KC (Central Asian Institute for Applied Geosciences, 2008), KN(I. Kyrgyz Institute of Seismology & University of California, 1991), KR (K. Kyrgyz Institute of Seismology, 2007), TJ (Geophysical Survey of the National Academy of sciences of Tajikistan, 2009), XP 2005–2007 (Roecker, 2005), XW 1997–2001 (Roecker et al., 1997), Y2 2007–2011 (Roecker & Levin, 2007), YT 2001 (Poupinet et al., 2001). The detailed earthquake and station information are listed in Tables S2 and S3 in Supporting Information S1. The waveform data of the earthquakes (including earthquake information) and Empirical Green's Functions (EGFs) used in this study are available at Gao (2024).

Acknowledgments

We gratefully acknowledge fruitful discussions with Kai Wang, Felix M. Schneider and Sébastien Chevrot. This work was supported by the Swiss National Supercomputing Center (CSCS) in the form of computing time Grants s868. The authors also gratefully acknowledge the Earth System Modelling Project (ESM) for funding this work by providing computing time on the ESM partition of the supercomputer JUWELS (Jülich Supercomputing Centre, 2021) at the Jülich Supercomputing Centre (JSC). We thank the operators of all networks used (full list see Open Research statement), most of them acquired with extended fieldwork efforts in harsh terrain. We are very grateful to the editor Fenglin Niu, the reviewer Chao Lvy and one anonymous reviewer for thorough reviews and appraisal. Open Access funding enabled and organized by Projekt DEAL.

References

Acosta, R., Kufner, S.-K., Yuan, X., & Rietbrock, A. (2023). The Moho anatomy of a continental subduction system (Hindu Kush Region, Afghanistan) illuminated by receiver functions. In *Presented at the AGU Fall Meeting 2023. (Abstract T43E-031)*.

Afanasiev, M., Boehm, C., Van Driel, M., Krischer, L., Rietmann, M., May, D. A., et al. (2019). Modular and flexible spectral-element waveform modelling in two and three dimensions. *Geophysical Journal International*, *216*(3), 1675–1692. https://doi.org/10.1093/gji/ggy469

Albuquerque Seismological Laboratory (ASL)/USGS. (1988). Global seismograph network (GSN - IRIS/USGS) [Dataset]. *International Federation of Digital Seismograph Networks*. https://doi.org/10.7914/SN/IU

Bloch, W., Metzger, S., Schurr, B., Yuan, X., Ratschbacher, L., Reuter, S., et al. (2023). The 2015-2017 Pamir earthquake sequence: Foreshocks, main shocks and aftershocks, seismotectonics, fault interaction and fluid processes. *Geophysical Journal International*, *233*(1), 641–662. https://doi.org/10.1093/gji/ggac473

Bloch, W., Schurr, B., Yuan, X., Ratschbacher, L., Reuter, S., Kufner, S.-K., et al. (2021). Structure and stress field of the lithosphere between Pamir and Tarim. *Geophysical Research Letters*, *48*(22), e2021GL095413. https://doi.org/10.1029/2021GL095413

Blom, N., Boehm, C., & Fichtner, A. (2017). Synthetic inversions for density using seismic and gravity data. *Geophysical Journal International*, *209*(2), 1204–1220. https://doi.org/10.1093/gji/ggx076

Bonvalot, S., Balmino, G., Briais, A., Kuhn, M., Peyrefitte, A., Vales, N., et al. (2012). *World Gravity Map, 1: 50000000 map, Eds (Tech. Rep.)*. BGI-CGMW-CNES-IRD, Paris.

Burtman, V. S. (2015). Tectonics and geodynamics of the Tian Shan in the Middle and Late Paleozoic. *Geotectonics*, *49*(4), 302–319. https://doi.org/10.11134/S0016852115040020

Burtman, V. S., & Molnar, P. (1993). Geological and geophysical evidence for deep subduction of continental crust beneath the Pamir. *Special Paper of the Geological Society of America*, *281*, 1–76. https://doi.org/10.1130/SPE281-P1

Central Asian Institute for Applied Geosciences. (2008). Central asian seismic network of CAIAG [Dataset]. *International Federation of Digital Seismograph Networks*. https://doi.org/10.17914/SN/KC

Chapman, J. B., Carrapa, B., DeCelles, P. G., Worthington, J., Mancin, N., Cobianchi, M., et al. (2020). The Tajik Basin: A composite record of sedimentary basin evolution in response to tectonics in the Pamir. *Basin Research*, *32*(3), 525–545. https://doi.org/10.1111/BRE.12381

Chapman, J. B., Scoggin, S. H., Kapp, P., Carrapa, B., Ducea, M. N., Worthington, J., et al. (2018). Mesozoic to Cenozoic magmatic history of the Pamir. *Earth and Planetary Science Letters*, *482*, 181–192. https://doi.org/10.11016/j.epsl.2017.10.041

Chen, M., Niu, F., Liu, Q., Tromp, J., & Zheng, X. (2015). Multiparameter adjoint tomography of the crust and upper mantle beneath East Asia: 1. Model construction and comparisons. *Journal of Geophysical Research: Solid Earth*, *120*(3), 1762–1786. https://doi.org/10.1002/2014JB011638

Dziewonski, A. M., & Anderson, D. L. (1981). Preliminary reference Earth model. *Physics of the Earth and Planetary Interiors*, *25*(4), 297–356. https://doi.org/10.1016/0031-9201(81)90046-7

Ekström, G., Nettles, M., & Dziewoński, A. (2012). The global CMT project 2004–2010: Centroid-moment tensors for 13,017 earthquakes. *Physics of the Earth and Planetary Interiors*, *200–201*, 1–9. https://doi.org/10.1016/j.pepi.2012.04.002

Fichtner, A., Kennett, B. L., Igel, H., & Bunge, H.-P. (2010). Full waveform tomography for radially anisotropic structure: New insights into present and past states of the Australasian upper mantle. *Earth and Planetary Science Letters*, *290*(3–4), 270–280. https://doi.org/10.1016/j.epsl.2009.12.003

Fichtner, A., Kennett, B. L. N., Igel, H., & Bunge, H.-P. (2008). Theoretical background for continental- and global-scale full-waveform inversion in the time–frequency domain. *Geophysical Journal International*, *175*(2), 665–685. https://doi.org/10.1111/j.1365-246X.2008.03923.x

Fichtner, A., & Leeuwen, T. V. (2015). Resolution analysis by random probing. *Journal of Geophysical Research: Solid Earth*, *120*(8), 5549–5573. https://doi.org/10.1002/2015JB012106

Fichtner, A., & Trampert, J. (2011). Resolution analysis in full waveform inversion. *Geophysical Journal International*, *187*(3), 1604–1624. https://doi.org/10.1111/j.1365-246X.2011.05218.x

Gao, Y. (2024). Waveform data of the empirical Green's functions (EGFs) and earthquakes for the manuscript "unraveling the mantle dynamics in central Asia with full waveform inversion tomography" [Dataset]. *Zenodo*. https://doi.org/10.5281/zenodo.13177444

Gao, Y., Tilmann, F., & Rietbrock, A. (2023). A review of misfit functions for adjoint full waveform inversion in seismology. *Geophysical Journal International*, *235*(3), 2794–2827. https://doi.org/10.11093/gji/ggad372

Gao, Y., Tilmann, F., van Herwaarden, D.-P., Thrastarson, S., Fichtner, A., Heit, B., et al. (2021a). Full waveform inversion beneath the Central Andes: Insight into the dehydration of the Nazca slab and delamination of the back-arc lithosphere. *Journal of Geophysical Research: Solid Earth*, *126*(7), e2021JB021984. https://doi.org/10.1029/2021JB021984

Gao, Y., Yuan, X., Heit, B., Tilmann, F., van Herwaarden, D.-P., Thrastarson, S., et al. (2021b). Impact of the Juan Fernandez ridge on the Pampean flat subduction inferred from full waveform inversion. *Geophysical Research Letters*, *48*(21), e2021GL095509. https://doi.org/10.1029/2021GL095509

Ge, J., Shi, X., Chen, H., Lin, X., Ge, W., Wei, X., et al. (2022). Two kinematic transformations of the Pamir salient since the Mid-Cenozoic: Constraints from multi-timescale deformation analysis. *Frontiers in Earth Science*, *10*, 967529. https://doi.org/10.3389/feart.2022.967529

GEOFON Data Centre. (1993). GEOFON seismic network [Dataset]. *Deutsches GeoForschungsZentrum GFZ*. https://doi.org/10.14470/TR560404

Geophysical Survey of the National Academy of sciences of Tajikistan. (2009). Tajikistan national seismic network [Dataset]. *International Federation of Digital Seismograph Networks*. https://doi.org/10.17914/SN/TJ

Gilligan, A., Roecker, S. W., Priestley, K. F., & Nunn, C. (2014). Shear velocity model for the Kyrgyz Tien Shan from joint inversion of receiver function and surface wave data. *Geophysical Journal International*, *199*(1), 480–498. https://doi.org/10.1093/gji/ggu225

Haberland, C., Wetzel, H.-U., Schurr, B., Abdybachaev, U., Orunbaev, S., & Sharshebaev, A. (2009). FERGHANA project [Dataset]. *GFZ Data Services*. https://doi.org/10.14470/1P035555

Hacker, B. R., Peacock, S. M., Abers, G. A., & Holloway, S. D. (2003). Subduction factory 2. Are intermediate-depth earthquakes in subducting slabs linked to metamorphic dehydration reactions? *Journal of Geophysical Research*, *108*(B1), 2030. https://doi.org/10.1029/2001JB001129

Hacker, B. R., Ratschbacher, L., Rutte, D., Stearns, M. A., Malz, N., Stübner, K., et al. (2017). Building the Pamir-Tibet Plateau—Crustal stacking, extensional collapse, and lateral extrusion in the Pamir: 3. Thermobarometry and petrochronology of deep Asian crust. *Tectonics*, *36*(9), 1743–1766. https://doi.org/10.11002/2017TC004488

Hirt, C., & Rexer, M. (2015). Earth2014: 1 arc-min shape, topography, bedrock and ice-sheet models – Available as gridded data and degree-10,800 spherical harmonics. *International Journal of Applied Earth Observation and Geoinformation*, *39*, 103–112. https://doi.org/10.1016/j.jag.2015.03.001

Huang, G.-C. D., Roecker, S. W., Levin, V., Wang, H., & Li, Z. (2016). Dynamics of intra-continental convergence between the western Tarim basin and central Tien Shan constrained by centroid moment tensors of regional earthquakes. *Geophysical Journal International*, *ggw415*(1), 561–576. https://doi.org/10.1093/gji/ggw415

Institut de physique du globe de Paris (IPGP), & Ecole et Observatoire des Sciences de la Terre de Strasbourg (EOST). (1982). GEOSCOPE, French global network of broad band seismic stations [Dataset]. *Institut de physique du globe de Paris (IPGP), Université de Paris*. https://doi.org/10.18715/GEOSCOPE.G

Institute of Geophysics China Earthquake Administration (IGPCEA). (2000). China national seismic network, Data Management Centre of China National Seismic Network at Institute of Geophysics, CEA [Dataset]. *International Federation of Digital Seismograph Networks*. https://doi.org/10.7914/SN/CB

Jiang, C., & Denolle, M. A. (2020). Noisepy: A new high-performance python tool for ambient-noise seismology. *Seismological Research Letters*, *91*(3), 1853–1866. https://doi.org/10.11785/0220190364

Jülich Supercomputing Centre. (2021). JUWELS cluster and booster: Exascale pathfinder with modular supercomputing architecture at Juelich supercomputing centre. *Journal of Large-Scale Research Facilities*, *7*(A138), A183. https://doi.org/10.17815/jlsrf-7-183

Koelemeijer, P., Ritsema, J., Deuss, A., & van Heijst, H.-J. (2015). SP12RTS: A degree-12 model of shear- and compressional-wave velocity for Earth's mantle. *Geophysical Journal International*, *204*(2), 1024–1039. https://doi.org/10.1093/gji/ggv481

Komatitsch, D., & Tromp, J. (2002). Spectral-element simulations of global seismic wave propagation—I. Validation. *Geophysical Journal International*, *149*(2), 390–412. https://doi.org/10.1046/j.1365-246X.2002.01653.x

Koulakov, I., & Sobolev, S. V. (2006). A tomographic image of Indian lithosphere break-off beneath the Pamir–Hindukush region. *Geophysical Journal International*, *164*(2), 425–440. https://doi.org/10.1111/j.1365-246X.2005.02841.x

Krischer, L., Fichtner, A., Boehm, C., & Igel, H. (2018). Automated large-scale full seismic waveform inversion for North America and the North Atlantic. *Journal of Geophysical Research: Solid Earth*, *123*(7), 5902–5928. https://doi.org/10.1029/2017JB015289

Krischer, L., Megies, T., Barsch, R., Beyreuther, M., Lecocq, T., Caudron, C., & Wassermann, J. (2015). ObsPy: A bridge for seismology into the scientific python ecosystem. *Computational Science & Discovery*, *8*(1), 014003. https://doi.org/10.1088/1749-4699/8/1/014003

Kristeková, M., Kristek, J., & Moczo, P. (2009). Time-frequency misfit and goodness-of-fit criteria for quantitative comparison of time signals. *Geophysical Journal International*, *178*(2), 813–825. https://doi.org/10.1111/j.1365-246X.2009.04177.x

Kufner, S.-K., Bie, L., Gao, Y., Lindner, M., Waizy, H., Kakar, N., & Rietbrock, A. (2023). The devastating 2022 M6.2 Afghanistan earthquake: Challenges, processes, and implications. *Geophysical Research Letters*, *50*(11), e2022GL102176. https://doi.org/10.1029/2022GL102176

Kufner, S.-K., Kakar, N., Bezada, M., Bloch, W., Metzger, S., Yuan, X., et al. (2021). The Hindu Kush slab break-off as revealed by deep structure and crustal deformation. *Nature Communications*, *12*, 1–11. https://doi.org/10.11038/s41467-021-21760-w

Kufner, S.-K., Kakar, N., Murodkulov, S., Schurr, B., Yuan, X., Rezai, T., & Shamal, S. (2018). TIPTIMON (Tien Shan-Pamir Monitoring Program) AFGHANISTAN 2 [Dataset]. *GFZ Data Services*. https://doi.org/10.14470/9P7562848989

Kufner, S.-K., Schurr, B., Haberland, C., Zhang, Y., Saul, J., Ischuk, A., & Oimahmadov, I. (2017). Zooming into the Hindu Kush slab break-off: A rare glimpse on the terminal stage of subduction. *Earth and Planetary Science Letters*, *461*, 127–140. https://doi.org/10.11016/j.epsl.2016.12.043

Kufner, S.-K., Schurr, B., Ratschbacher, L., Murodkulov, S., Abdulhameed, S., Ischuk, A., et al. (2018). Seismotectonics of the Tajik basin and surrounding mountain ranges. *Tectonics*, *37*(8), 2404–2424. https://doi.org/10.1029/2017TC004812

Kufner, S.-K., Schurr, B., Sippl, C., Yuan, X., Ratschbacher, L., Akbar, M., et al. (2016). Deep India meets deep Asia: Lithospheric indentation, delamination and break-off under Pamir and Hindu Kush (Central Asia). *Earth and Planetary Science Letters*, *435*, 171–184. https://doi.org/10.11016/j.epsl.2015.11.046

Kumar, V., Rai, S. S., Hawkins, R., & Bodin, T. (2022). Seismic imaging of crust beneath the western Tibet-Pamir and Western Himalaya using ambient noise and earthquake data. *Journal of Geophysical Research: Solid Earth*, *127*(6), e2021JB022574. https://doi.org/10.11029/2021JB022574

Kyrgyz Institute of Seismology, I., & University of California, S. D. (1991). Kyrgyz seismic telemetry network [Dataset]. *International Federation of Digital Seismograph Networks*. https://doi.org/10.17914/SN/KN

Kyrgyz Institute of Seismology, K. (2007). Kyrgyz digital network [Dataset]. *International Federation of Digital Seismograph Networks*. https://doi.org/10.17914/SN/KR

Laske, G., Masters, G., Ma, Z., & Pasyanos, M. (2013). Update on CRUST1. 0—A 1-degree global model of Earth's crust. In *Geophys. Res. Abstracts, 15, Abstract EGU2013-2658*.

Li, W., Chen, Y., Tan, P., & Yuan, X. (2020). Geodynamic processes of the continental deep subduction: Constraints from the fine crustal structure beneath the Pamir plateau. *Science China Earth Sciences*, *63*(5), 649–661. https://doi.org/10.1007/s11430-019-9587-3

Li, W., Chen, Y., Yuan, X., Schurr, B., Mechie, J., Oimahmadov, I., & Fu, B. (2018). Continental lithospheric subduction and intermediate-depth seismicity: Constraints from S-wave velocity structures in the Pamir and Hindu Kush. *Earth and Planetary Science Letters*, *482*, 478–489. https://doi.org/10.11016/j.epsl.2017.11.031

Li, W., Chen, Y., Yuan, X., Xiao, W., & Windley, B. F. (2022). Intracontinental deformation of the Tianshan Orogen in response to India-Asia collision. *Nature Communications 2022*, *13*(1), 1–8. https://doi.org/10.11038/s41467-022-30795-6

Li, Z., Roecker, S., Li, Z., Wei, B., Wang, H., Schelochkov, G., & Bragin, V. (2009). Tomographic image of the crust and upper mantle beneath the western tien Shan from the manas broadband deployment: Possible evidence for lithospheric delamination. *Tectonophysics*, *477*(1), 49–57. https://doi.org/10.1016/j.tecto.2009.05.007

Liang, Y., Li, L., Liao, J., & Gao, R. (2020). Interaction of the Indian and Asian Plates under the Pamir and Hindu-Kush Regions: Insights from 3-D shear wave velocity and anisotropic structures. *Geochemistry, Geophysics, Geosystems*, *21*(8), 1–15. https://doi.org/10.11029/2020GC009041

Liao, J., Gerya, T., Thielmann, M., Webb, A. A. G., Kufner, S.-K., & Yin, A. (2017). 3D geodynamic models for the development of opposing continental subduction zones: The Hindu Kush–Pamir example. *Earth and Planetary Science Letters*, *480*, 133–146. https://doi.org/10.11016/j.epsl.2017.10.005

Liu, D. C., & Nocedal, J. (1989). On the limited memory BFGS method for large scale optimization. *Mathematical Programming*, *45*(1), 503–528. https://doi.org/10.1007/BF01589116

Lu, Y., Stehly, L., Brossier, R., & Paul, A. (2020). Imaging Alpine crust using ambient noise wave-equation tomography. *Geophysical Journal International*, *222*(1), 69–85. https://doi.org/10.1093/gji/ggaa145

Lü, Z., Gao, H., & Lei, J. (2020). New insight into crustal and lithospheric variability beneath the central Tien Shan (NW China) revealed by P-wave receiver functions. *Journal of Asian Earth Sciences*, *189*, 104187. https://doi.org/10.11016/j.jseaes.2019.104187

Lü, Z., Gao, H., Lei, J., Yang, X., Rathnayaka, S., & Li, C. (2019). Crustal and upper mantle structure of the Tien Shan orogenic belt from full-wave ambient noise tomography. *Journal of Geophysical Research: Solid Earth*, *124*(4), 3987–4000. https://doi.org/10.11029/2019JB017387

Lü, Z., Lei, J., Zhao, L., Fu, X., Chen, J., Li, G., & Kong, Q. (2021). Crustal deformation of intermontane basins beneath Central Tien Shan revealed by full-wave ambient noise tomography. *Tectonophysics*, *821*, 229143. https://doi.org/10.1016/j.tecto.2021.229143

Mechie, J., Schurr, B., Yuan, X., Schneider, F., Sippl, C., Minaev, V., et al. (2019). Observations of guided waves from the Pamir seismic zone provide additional evidence for the existence of subducted continental lower crust. *Tectonophysics*, *762*, 1–16. https://doi.org/10.11016/j.tecto.2019.04.007

Mohadjer, S., Ehlers, T. A., Bendick, R., Stübner, K., & Strube, T. (2016). A quaternary fault database for central Asia. *Natural Hazards and Earth System Sciences*, *16*(2), 529–542. https://doi.org/10.5194/nhess-16-529-2016

Molnar, P., & Bendick, R. (2019). Seismic moments of intermediate-depth earthquakes beneath the Hindu Kush: Active stretching of a blob of sinking thickened mantle lithosphere? *Tectonics*, *38*(5), 1651–1665. https://doi.org/10.1029/2018TC005336

Najman, Y., Appel, E., Boudagher-Fadel, M., Bown, P., Carter, A., Garzanti, E., et al. (2010). Timing of India-Asia collision: Geological, biostratigraphic, and palaeomagnetic constraints. *Journal of Geophysical Research*, *115*(B12), B12416. https://doi.org/10.1029/2010JB007673

Nouibat, A., Brossier, R., Stehly, L., Cao, J., Paul, A., Team, C., & Group, A. W. (2023). Ambient-noise wave-equation tomography of the Alps and Ligurian-Provence Basin [Dataset]. *Journal of Geophysical Research: Solid Earth*, *128*(10). https://doi.org/10.1029/2023GL108018. e2023JB026776.

Panning, M., & Romanowicz, B. (2006). A three-dimensional radially anisotropic model of shear velocity in the whole mantle. *Geophysical Journal International*, *167*(1), 361–379. https://doi.org/10.1111/j.1365-246X.2006.03100.x

Pavlis, N. K., Holmes, S. A., Kenyon, S. C., & Factor, J. K. (2012). The development and evaluation of the Earth Gravitational Model 2008 (EGM2008). *Journal of Geophysical Research*, *117*(B4), B04406. https://doi.org/10.1029/2011JB008916

Perry, M., Kakar, N., Ischuk, A., Metzger, S., Bendick, R., Molnar, P., & Mohadjer, S. (2019). Little geodetic evidence for localized Indian subduction in the Pamir-Hindu Kush of Central Asia. *Geophysical Research Letters*, *46*(1), 109–118. https://doi.org/10.1029/2018GL080065

Płonka, A., Blom, N., & Fichtner, A. (2016). The imprint of crustal density heterogeneities on regional seismic wave propagation. *Solid Earth*, *7*(6), 1591–1608. https://doi.org/10.5194/se-7-1591-2016

Poupinet, G., Wittlinger, G., & Antenna, R.-S. M. (2001). 2001 WEST KUNLUN Broadband and short period temporary experiment (RESIF - SISMOB) [Dataset]. *RESIF - Réseau Sismologique et géodésique Français*. https://doi.org/10.15778/RESIF.YT2001

Replumaz, A., Negredo, A. M., Guillot, S., & Villaseñor, A. (2010). Multiple episodes of continental subduction during India/Asia convergence: Insight from seismic tomography and tectonic reconstruction. *Tectonophysics*, *483*(1–2), 125–134. https://doi.org/10.1016/j.tecto.2009.10.007

Robinson, A. C., Ducea, M., & Lapen, T. J. (2012). Detrital zircon and isotopic constraints on the crustal architecture and tectonic evolution of the northeastern Pamir. *Tectonics*, *31*(2), TC2016. https://doi.org/10.1029/2011TC003013

Rodgers, A. J., Doody, C. D., & Fichtner, A. (2024). WUS324: Multiscale full waveform inversion approaching convergence improves waveform fits while imaging seismic structure of the western United States. *Geophysical Research Letters*, *51*(20), e2024GL110911. https://doi.org/10.1029/2024GL110911

Roecker, S. (2005). Discrete vs. continuous continental deformation and the role of the lower crust in the Tien Shan [Dataset]. *International Federation of Digital Seismograph Networks*. https://doi.org/10.17914/SN/XP_2005

Roecker, S., & Levin, V. (2007). Collaborative research: Imaging the upper mantle beneath the Western Tibetan Plateau [Dataset]. *International Federation of Digital Seismograph Networks*. https://doi.org/10.17914/SN/Y2_2007

Roecker, S., Pavlis, G., & Vernon, F. (1997). Multidisciplinary investigation of the mountain building in the Tien Shan [Dataset]. *International Federation of Digital Seismograph Networks*. https://doi.org/10.17914/SN/XW_1997

Ruan, Y., Lei, W., Modrak, R., Örsvuran, R., Bozdag, E., & Tromp, J. (2019). Balancing unevenly distributed data in seismic tomography: A global adjoint tomography example. *Geophysical Journal International*, *219*(2), 1225–1236. https://doi.org/10.1093/gji/ggz356

Rutte, D., Ratschbacher, L., Khan, J., Stübner, K., Hacker, B. R., Stearns, M. A., et al. (2017). Building the Pamir-Tibetan Plateau—Crustal stacking, extensional collapse, and lateral extrusion in the Central Pamir: 2. Timing and rates. *Tectonics*, *36*(3), 385–419. https://doi.org/10.1002/2016TC004294

Sass, P., Ritter, O., Ratschbacher, L., Tympel, J., Matiukov, V. E., Rybin, A. K., & Batalev, V. Y. (2014). Resistivity structure underneath the Pamir and Southern Tian Shan. *Geophysical Journal International*, *198*(1), 564–579. https://doi.org/10.11093/gji/ggu146

Schmidt, J., Hacker, B. R., Ratschbacher, L., Stübner, K., Stearns, M., Kylander-Clark, A., et al. (2011). Cenozoic deep crust in the Pamir. *Earth and Planetary Science Letters*, *312*(3–4), 411–421. https://doi.org/10.1016/j.epsl.2011.10.034

Schneider, F., Yuan, X., Schurr, B., Mechie, J., Sippl, C., Haberland, C., et al. (2013). Seismic imaging of subducting continental lower crust beneath the Pamir. *Earth and Planetary Science Letters*, *375*, 101–112. https://doi.org/10.11016/j.epsl.2013.05.015

Schneider, F., Yuan, X., Schurr, B., Mechie, J., Sippl, C., Kufner, S., et al. (2019). The crust in the Pamir: Insights from receiver functions. *Journal of Geophysical Research: Solid Earth*, *124*, 9313–9331. https://doi.org/10.11029/2019JB017765

Schurr, B., Ratschbacher, L., Sippl, C., Gloaguen, R., Yuan, X., & Mechie, J. (2014). Seismotectonics of the Pamir. *Tectonics*, *33*(8), 1501–1518. https://doi.org/10.1002/2014TC003576

Schurr, B., Yuan, X., Haberland, C., Mechie, J., & Kufner, S.-K. (2012). TIPTIMON (Tien Shan-Pamir monitoring program) TAJIKISTAN (2012/2014) [Dataset]. *GFZ Data Services*. https://doi.org/10.11470/0P7567352807

Schurr, B., Yuan, X., Haberland, C., Mechie, J., & Kufner, S.-K. (2013). TIPTIMON (Tien Shan-Pamir monitoring program) AFGHANISTAN (2013/2014) [Dataset]. *GFZ Data Services*. https://doi.org/10.14470/1P7568352842

Schurr, B., Yuan, X., Kufner, S., & Bloch, W. (2017). Sarez Pamir aftershock seismic network [Dataset]. *GFZ Data Services*. https://doi.org/10.14470/4U7561589984

Schwab, M., Ratschbacher, L., Siebel, W., McWilliams, M., Minaev, V., Lutkov, V., et al. (2004). Assembly of the Pamirs: Age and origin of magmatic belts from the southern Tien Shan to the southern Pamirs and their relation to Tibet. *Tectonics*, *23*(4), TC4002. https://doi.org/10.1029/2003TC001583

Scripps Institution of Oceanography. (1986). Global Seismograph Network - IRIS/IDA [Dataset]. *International Federation of Digital Seismograph Networks*. https://doi.org/10.17914/SN/II

Shaffer, M., Hacker, B. R., Ratschbacher, L., & Kylander-Clark, A. R. (2017). Foundering triggered by the collision of India and Asia captured in xenoliths. *Tectonics*, *36*(10), 1913–1933. https://doi.org/10.11002/2017TC004704

Sippl, C., Schurr, B., Tympel, J., Angiboust, S., Mechie, J., Yuan, X., et al. (2013). Deep burial of Asian continental crust beneath the Pamir imaged with local earthquake tomography. *Earth and Planetary Science Letters*, *384*, 165–177. https://doi.org/10.11016/j.epsl.2013.10.013

Tang, G. J., Wyman, D. A., Dan, W., Wang, Q., Liu, X. J., Yang, Y. N., et al. (2024). Protracted and progressive crustal melting during continental collision in the Pamir and Plateau growth. *Journal of Petrology*, *65*(4). https://doi.org/10.1093/petrology/egae024

Tao, K., Grand, S. P., & Niu, F. (2017). Full-waveform inversion of triplicated data using a normalized-correlation-coefficient-based misfit function. *Geophysical Journal International*, *210*(3), 1517–1524. https://doi.org/10.1093/gji/ggx249

Tao, K., Grand, S. P., & Niu, F. (2018). Seismic structure of the upper mantle beneath eastern Asia from full waveform seismic tomography. *Geochemistry, Geophysics, Geosystems*, *19*(8), 2732–2763. https://doi.org/10.1029/2018GC007460

Treloar, P. J., & Izatt, C. N. (1993). Tectonics of the Himalayan collision between the Indian plate and the Afghan block: A synthesis. *Geological Society, London, Special Publications*, *74*(1), 69–87. https://doi.org/10.1144/GSL.SP.1993.074.01.06

Waldhör, M., Appel, E., Frisch, W., & Patzelt, A. (2001). Palaeomagnetic investigation in the Pamirs and its tectonic implications. *Journal of Asian Earth Sciences*, *19*(4), 429–451. https://doi.org/10.1016/S1367-9120(00)00030-4

Wang, K., Yang, Y., Basini, P., Tong, P., Tape, C., & Liu, Q. (2018). Refined crustal and uppermost mantle structure of southern California by ambient noise adjoint tomography. *Geophysical Journal International*, *215*(2), 844–863. https://doi.org/10.11093/gji/ggy312

Wehner, D., Blom, N., Rawlinson, N., Daryono, Böhm, C., Miller, M. S., et al. (2022). SASSY21: A 3-D seismic structural model of the lithosphere and underlying mantle beneath southeast Asia from multi-scale adjoint waveform tomography. *Journal of Geophysical Research: Solid Earth*, *127*(3), e2021JB022930. https://doi.org/10.1029/2021JB022930

Worthington, J. R., Ratschbacher, L., Stübner, K., Khan, J., Malz, N., Schneider, S., et al. (2020). The Alichur Dome, south Pamir, western India–Asia collisional zone: Detailing the Neogene Shakhdara–Alichur Syn-collisional Gneiss-Dome complex and connection to lithospheric processes. *Tectonics*, *39*(1), e2019TC005735. https://doi.org/10.11029/2019TC005735

Xiao, W., Huang, B., Han, C., Sun, S., & Li, J. (2010). A review of the western part of the Altaids: A key to understanding the architecture of accretionary orogens. *Gondwana Research*, *18*(2–3), 253–273. https://doi.org/10.11016/j.gr.2010.01.007

Xiao, W., Windley, B. F., Allen, M. B., & Han, C. (2013). Paleozoic multiple accretionary and collisional tectonics of the Chinese Tianshan orogenic collage. *Gondwana Research*, *23*(4), 1316–1341. https://doi.org/10.11016/j.gr.2012.01.012

Xu, Q., Zhao, J., Yuan, X., Liu, H., Ju, C., Schurr, B., & Bloch, W. (2021). Deep crustal contact between the Pamir and Tarim Basin deduced from receiver functions. *Geophysical Research Letters*, *48*(9), e2021GL093271. https://doi.org/10.11029/2021GL093271

Xu, Y., Li, Z., & Roecker, S. W. (2007). Uppermost mantle structure and its relation with seismic activity in the central Tien Shan. *Geophysical Research Letters*, *34*(10), L10304. https://doi.org/10.1029/2007GL029708

Yin, A., Nie, S., Craig, P., Harrison, T. M., Ryerson, F. J., Xianglin, Q., & Geng, Y. (1998). Late Cenozoic tectonic evolution of the southern Chinese Tian Shan. *Tectonics*, *17*, 1–27. https://doi.org/10.11029/97TC03140

Yuan, H., Romanowicz, B., Fischer, K. M., & Abt, D. (2011). 3-D shear wave radially and azimuthally anisotropic velocity model of the North American upper mantle. *Geophysical Journal International*, *184*(3), 1237–1260. https://doi.org/10.1111/j.1365-246X.2010.04901.x

Yuan, X., Mechie, J., & Schurr, B. (2008). Tienshan Pamir Geodynamics Project (TIPAGE) [Dataset]. *Deutsches GeoForschungsZentrum GFZ*. https://doi.org/10.14470/2O097102

Yuan, X., Schurr, B., Bloch, W., Xu, Q., & Zhao, J. (2017). East Pamir Network [Dataset]. *GFZ Data Services*. https://doi.org/10.14470/3U7560589977

Yuan, Y., Bozdağ, E., Ciardelli, C., Gao, F., & Simons, F. J. (2020). The exponentiated phase measurement, and objective-function hybridization for adjoint waveform tomography. *Geophysical Journal International*, *221*(2), 1145–1164. https://doi.org/10.1093/gji/ggaa063

Zhang, B., Bao, X., & Xu, Y. (2020). Distinct orogenic processes in the south- and north-central Tien Shan from receiver functions. *Geophysical Research Letters*, *47*(6), 1–8. https://doi.org/10.11029/2019GL086941

Zhu, H., Bozdağ, E., & Tromp, J. (2015). Seismic structure of the European upper mantle based on adjoint tomography. *Geophysical Journal International*, *201*(1), 18–52. https://doi.org/10.1093/gji/ggu492

Zhu, H., Komatitsch, D., & Tromp, J. (2017). Radial anisotropy of the North American upper mantle based on adjoint tomography with USArray. *Geophysical Journal International*, *211*(1), 349–377. https://doi.org/10.1093/gji/ggx305